Fire in the Heart: A Characterization of the High Kinetic Temperatures and Heating Sources in the Nucleus of NGC 253

Mangum, J.G.; Ginsburg, A.G.; Henkel, C.; Menten, K.M.; Aalto, S.; Werf, P.P. van der

Fire in the Heart: A Characterization of the High Kinetic Temperatures and
Heating Sources in the Nucleus of NGC 253

Jeffrey G. Mangum,[1] Adam G. Ginsburg,[2, *] Christian Henkel,[3, 4]
Karl M. Menten,[3] Susanne Aalto,[5] and Paul van der Werf[6]

[1] National Radio Astronomy Observatory, 520 Edgemont Road, Charlottesville, VA 22903-2475, USA

[2] National Radio Astronomy Observatory, P.O. Box O, 1003 Lopezville Road Socorro, NM 87801-0387, USA

[3] Max-Planck-Institut für Radioastronomie, Auf dem Hügel 69, 53121 Bonn, Germany

[4] Astronomy Department, Faculty of Science, King Abdulaziz University, P. O. Box 80203, Jeddah, Saudi Arabia

[5] Department of Earth and Space Sciences, Chalmers University of Technology, Onsala Observatory, SE-439 92 Onsala, Sweden

[6] Leiden Observatory, Leiden University, 2300 RA, Leiden, The Netherlands

ABSTRACT

The nuclear starburst within the central $\sim 15''$ ($\sim 250\,$pc; $1'' \simeq 17\,$pc) of NGC 253 has been extensively studied as a prototype for the starburst phase in galactic evolution. Atacama Large Millimeter/submillimeter Array (ALMA) imaging within receiver Bands 6 and 7 have been used to investigate the dense gas structure, kinetic temperature, and heating processes which drive the NGC 253 starburst. Twenty-nine transitions from fifteen molecular species/isotopologues have been identified and imaged at $1.''5$ to $0.''4$ resolution, allowing for the identification of five of the previously-studied giant molecular clouds (GMCs) within the central molecular zone (CMZ) of NGC 253. Ten transitions from the formaldehyde (H_2CO) molecule have been used to derive the kinetic temperature within the $\sim 0.''5$ to $5''$ dense-gas structures imaged. On $\sim 5''$ scales we measure $T_K \gtrsim 50\,$K, while on size scales $\lesssim 1''$ we measure $T_K \gtrsim 300\,$K. These kinetic temperature measurements further delineate the association between potential sources of dense gas heating. We have investigated potential heating sources by comparing our measurements to models which predict the physical conditions associated with dense molecular clouds that possess a variety of heating mechanisms. This comparison has been supplemented with tracers of recently-formed massive stars ($Br\gamma$) and shocks ([FeII]). Derived molecular column densities point to a radially-decreasing abundance of molecules with sensitivity to cosmic ray and me-

Corresponding author: Jeff Mangum
jmangum@nrao.edu

chanical heating within the NGC 253 CMZ. These measurements are consistent with radio spectral index calculations which suggest a higher concentration of cosmic ray producing supernova remnants within the central 10 pc of NGC 253.

1. INTRODUCTION

The comparison between the properties of the star formation process in our Galaxy to that found in galaxies which appear to be producing a plethora of stars over a relatively short time period is dramatic. Taking NGC 253 as the prototype for a starburst galaxy, the giant molecular clouds (GMCs) are $\sim 50\%$ larger, ~ 100 times more massive, have velocity dispersions that are ~ 10 times larger, and free-fall times ~ 3 times shorter than GMCs in the Milky Way disk[1]. With its relative proximity ($d = 3.5$ Mpc; Rekola et al. 2005) and optimal disk orientation of $\sim 76°$ (McCormick et al. 2013), which presents disk velocity excursions running from ~ 180 to ~ 300 km/s, NGC 253 provides an excellent perspective to Earthly observers of the extragalactic star formation process. As higher resolution and more sensitive infrared through millimeter measurements have become available, the spectral and structural complexity of the central kiloparsec of the NGC 253 molecular disk has become more apparent. Structures which are reminiscent of Milky Way massive star formation regions with spectral richness rivaling those measured toward hot core sources and our own Galactic Center region can now be measured and analyzed, providing valuable clues to the burst-mode of star formation in external galaxies.

Using the millimeter/submillimeter spatial and spectral properties measured toward NGC 253, we have endeavored to understand some basic properties of the star formation process in this galaxy. Specifically, what is the kinetic temperature within the dense gas which is in the process of forming stars, and what are the heating processes which drive those kinetic temperatures? Section 2 presents our ALMA frequency Band 6 and 7 spectral line emission measurements, from which the spatial (Section 3.2) and spectral (Section 4.1) properties have been derived. Molecular spectral line integrated intensities have been extracted using a python-based script (Section 4.2), from which molecular column densities have been derived (Section 6). Section 5 presents our analysis of the imaged transitions from the formaldehyde (H$_2$CO) molecule which have been used to derive the kinetic temperature within the identified GMCs which inhabit the NGC 253 nucleus. With this information, we then use the molecular abundances inferred from our measurements, in corporation with infrared through radio studies of the NGC 253 nuclear disk, to constrain chemi-

---

* National Radio Astronomy Observatory Jansky Fellow
[1] See Table 4 in Leroy et al. (2015) for an excellent comparison of physical properties in Milky Way disk and NGC 253 GMCs.

Table 1. Observations Summary

Band	Array	Obs Date/Start Time	t_{on} (minutes)	N_{ant}	Baselines (Min,Max) (m)
NGC 253, RA(J2000)=00:47:33.1339, Dec(J2000)=−25:17:19.68, V_{hel}=258.8 km/s					
6	12m	2014-12-28 23:57:24	6.8	38	(15,349)
6	12m	2015-05-02 16:18:28	38.1	34	(15,349)
6	ACA	2014-06-04 09:12:16	24.2	9	(9,49)
6	ACA	2014-06-04 10:17:53	24.2	9	(9,49)
6	ACA	2014-06-04 11:25:14	24.2	9	(9,49)
7	12m	2014-05-19 09:15:59	34.3	34	(21,650)
7	ACA	2014-05-19 10:20:02	32.8	8	(9,49)
7	ACA	2014-06-08 09:49:14	32.8	10	(9,49)

cal models which trace the influence of PDR, XDR, CRDR, and mechanical heating within dense molecular gas (Section 7). In Section 8 we discuss the anomalous spatial distributions presented by our measured CH_3OH and vibrationally-excited HC_3N and HNC transitions and their association with infrared and radio emission sources. We conclude with a discussion of the connection between potential sources of heating and the measured molecular abundances in the NGC 253 CMZ.

2. OBSERVATIONS

A single field was observed toward NGC 253 using the Atacama Large Millimeter Array (ALMA) 12m Array, Atacama Compact Array (ACA), and Total Power (TP) antennas at Bands 6 and 7 (ALMA projects 2013.1.00099.S and 2015.1.00476.S). The phase center was at RA(J2000)=00:47:33.1339, Dec(J2000)=−25:17:19.68, V_{hel}=258.8 km/s. ALMA standard observing routines were used for all three types of measurements, which included pointing, flux, and phase calibration measurements. The TP measurements have proven to be unusable due to incomplete telluric line removal encountered during processing in the Common Astronomy Software Applications (CASA) data reduction package. As we have not included these measurements in our analysis we provide no further information on them.

Tables 1 and 2 summarize the general observational characteristics of the ALMA Band 6 and 7 measurements of NGC 253 presented. Three separate spectral windows for each frequency band in these 12m Array and ACA measurements were employed. For the Band 6 measurements each spectral window spanned frequencies from 217.284692 to 219.159692 GHz, 218.971025 to 220.846025 GHz, and 233.7 to 235.7 GHz. For Band 7 the three separate spectral windows spanned frequencies from 350.831145 to 352.706145 GHz, 362.482149 to 364.357149 GHz, and 363.881785 to 365.756785 GHz. For the Band 6 measurements of NGC 253 the total on-source integration time (t_{on}) for each type of measurement was 44.9 min (12m Array) and

Table 2. Spectral Setup

Rest Frequency	Bandwidth	N_{chan}	Channel Width
(GHz)	(GHz)		(MHz and km/s)
ALMA Band 6 12m Array Correlator			
218.222192	1.875	960	1.953/2.686
219.908525	1.875	960	1.953/2.665
234.700	2.000	122	15.625/19.978
ALMA Band 6 ACA Correlator			
218.222192	1.992	1024	1.992/2.67
219.908525	1.992	1024	1.992/2.65
234.700	1.938	128	15.625/20.05
ALMA Band 7 12m Array Correlator			
351.768645	1.875	480	3.906/3.33
363.419649	1.875	480	3.906/3.33
364.819285	1.875	480	3.906/3.33
ALMA Band 7 ACA Correlator			
351.768645	1.992	510	3.906/3.33
363.419649	1.992	510	3.906/3.33
364.819285	1.992	510	3.906/3.33

72.6 min (ACA), for a 12m:ACA on-source integration time ratio of 1:1.6. At Band 7 the total on-source integration time toward NGC 253 for each type of measurement was 34.3 min (12m Array) and 65.6 min (ACA), for a 12m:ACA on-source integration time ratio of 1:1.9. Both on-source integration time ratios are consistent with the standard integration time ratio for ALMA observations acquired in Cycle 2 of 12m Array:ACA:TP = 1:2:4 (Mason & Brogan 2013).

Amplitude, bandpass, phase, and pointing calibration information for these measurements are listed in Appendix A (Table 11). For Band 6 gain and bandpass calibrator fluxes ranged from 253 to 688 mJy. Uncertainties in the Band 6 gain and bandpass calibrator measurements are in the range 0.4–1.7%. For Band 7 gain and bandpass calibrator fluxes ranged from 274 to 2244 mJy. Uncertainties in the Band 7 gain and bandpass calibrator measurements are with one exception in the range 0.1–3.9%. The Band 7 12m Array measurements on 2014-05-19 have higher gain calibration uncertainties which are in the range 4.3–6.4%.

At Band 6 flux calibration was effected using Uranus (28.9–34.8 Jy), Mars (78.5–89.5 Jy), and Neptune (13.0–13.6 Jy). Band 6 flux calibrator uncertainties are estimated to be 5% for Uranus (Orton et al. 2014), 10% for Mars (Perley & Butler 2013; Weiland et al. 2011), and 10% for Neptune (Müller et al. 2016). For Mars our estimate of the absolute flux uncertainty derives from the 1–50 GHz absolute flux (Perley & Butler 2013) and 23–93 GHz absolute brightness temperature (Weiland et al. 2011) measurements of Mars. For our absolute flux uncertainty estimate for Neptune we

have increased the nominal 5% uncertainty quoted by Müller et al. (2016) due to the presence of a CO absorption transition at 230.538 GHz present in the atmosphere of Neptune to 10%.

At Band 7 flux calibration was effected using J2258−2758 (390 mJy), Neptune (25.8–27.8 Jy), and Uranus (63.8–66.6 Jy). Band 7 flux calibrator uncertainties are estimated to be 10% for Neptune (Müller et al. 2016) and 5% for Uranus (Orton et al. 2014). As was done for our Band 6 measurements, for our absolute flux uncertainty estimate for Neptune we have increased the nominal 5% uncertainty quoted by Müller et al. (2016) due to the presence of a CO absorption transition at 345.796 GHz present in the atmosphere of Neptune. For unknown reasons the 12m Array measurements of NGC 253 at Band 7 employed a non-standard flux calibrator (J2258−2758). The ALMA Calibration Catalog lists the flux uncertainty for this quasar as 15%, but no further information regarding the time period over which this uncertainty applies is provided.

All measurements were either manually or pipeline calibrated by ALMA North American Regional Center staff using the CASA reduction package. Following delivery of each calibrated interferometric measurement group (12m Array and ACA), self-calibration was attempted to correct for residual phase errors. For all measurement groups at both Bands 6 and 7 one iteration of phase-only self-calibration utilizing a 60 second averaging time was used. The bright NGC 253 continuum source at Bands 6 and 7 was used as a self-calibration source, which resulted in signal-to-noise improvement by factors of 2.9 and 1.9 in the Band 6 continuum of our 12m Array and ACA data, and by factors of 3.0 and 3.5 in the Band 7 continuum of our 12m Array and ACA data, respectively.

3. RESULTS

3.1. *Imaging and Spectral Baseline Fitting*

Spectral cube imaging was performed using the CASA package. Images of each self calibrated spectral window image cube for NGC 253 were created using the `clean` task within CASA. An image may be characterized by the spatial frequencies which are well represented in it; these correspond to the regions in the Fourier transform ("uv" space) of the image which were well measured by the instrument. Interferometers generally cover a range of spatial frequencies which are limited by the longest and shortest baselines used in the interferometric measurement (see Table 1). Single antennas, in principle, measure all spatial frequencies down to those corresponding to the instrument reflector diameter. Ideally, images with overlapping, well-sampled spatial frequencies can be combined to derive an image which represents all the sampled spatial frequencies. "Feathering" is a technique by which images are combined in the uv plane to recover the spatial frequencies in the input images (Cotton 2017). Combination of the 12m Array and ACA measurements for each spectral window was done by employing the CASA-implementation of the feathering technique, using the

task `feather`. Table 3 lists the properties of each 12m Array, ACA, and feathered image cubes for each spectral window from our measurements of NGC 253.

Table 3. Spectral and Continuum Image Properties

Rest Frequency	Δv	$\theta_{maj} \times \theta_{min}$@PA[a]	RMS per Channel
(GHz)	(km/s)	(arcsec,arcsec,deg)	(mJy/beam)
NGC 253 Band 6 12m Array			
218.222192	5.5	1.52×0.87@+82.15	2.5
219.908525	5.5	1.56×0.89@+83.96	2.0
234.700	25.0	1.41×0.81@+82.28	0.9
NGC 253 Band 6 ACA			
218.222192	5.5	7.55×4.70@+78.94	12.5
219.908525	5.5	7.61×4.78@+79.08	10.0
234.700	25.0	7.19×4.32@+76.34	6.0
NGC 253 Band 6 12m Array and ACA Feather			
218.222192	5.5	1.52×0.87@+82.15	2.5
$\cdots$	55 (cont)	$\cdots$	0.8
219.908525	5.5	1.56×0.89@+83.96	1.8
$\cdots$	385 (cont)	$\cdots$	0.3
234.700	25.0	1.41×0.81@+82.28	0.9
$\cdots$	250 (cont)	$\cdots$	0.4
NGC 253 Band 7 12m Array			
351.768645	3.5	0.45×0.29@−85.64	2.0
363.419649	3.5	0.43×0.28@−85.94	2.8
364.819285	3.5	0.43×0.28@−86.00	3.0
NGC 253 Band 7 ACA			
351.768645	3.5	4.99×2.48@+79.58	13.5
363.419649	3.5	4.79×2.39@+78.17	13.5
364.819285	3.5	4.78×2.39@+78.96	22.0
NGC 253 Band 7 12m Array and ACA Feather			
351.768645	3.5	0.45×0.29@−85.64	2.0
$\cdots$	35 (cont)	$\cdots$	0.9
363.419649	3.5	0.43×0.28@−85.94	3.0
$\cdots$	35 (cont)	$\cdots$	0.8
364.819285	3.5	0.43×0.28@−86.00	3.2
$\cdots$	35 (cont)	$\cdots$	1.5

[a] Continuum beam parameters are the same as their corresponding spectral line cubes, thus have been omitted.
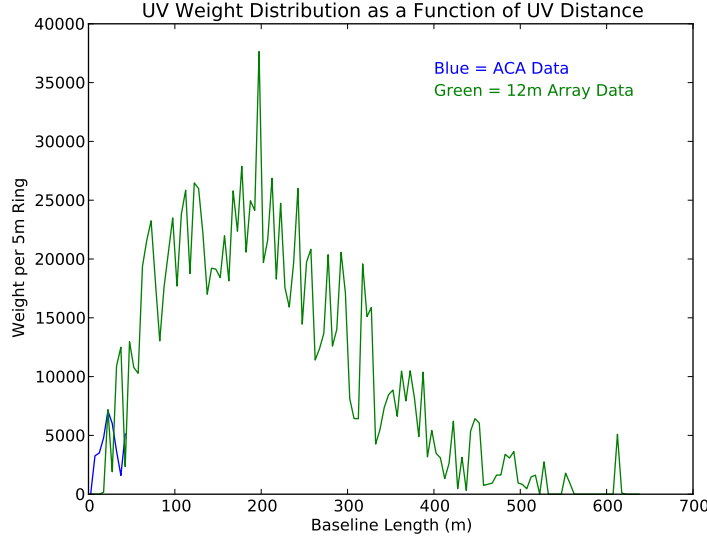
Figure 1. Annularly-averaged uv data weights as function of baseline length for the 351 GHz spectral window from our Band 7 12m Array and ACA measurements of NGC 253. The 12m Array and ACA uv data weights shown have been rescaled to place them on the same scale. This comparison suggests that the ACA data contributes minimally to the combined spatial frequency information in our imaging of NGC 253.

To assess the relative import of each contributing image cube to the combined (feathered) spectral image cube, we have plotted the uv data weights averaged over 5 m annuli in the uv-plane as a function of baseline length for corresponding 12m Array and ACA data sets from our measurements. Figure 1 shows the annularly-averaged uv data weights for the 12m Array and ACA measurements of our Band 7 spectral window near 351 GHz. This comparison shows that the ACA measurements contribute minimally to the overall spatial frequency sensitivity in our imaging measurements.

Due to the density of spectral lines in all of the spectral image cubes for NGC 253 (Figure 2 presents an example spectrum), spectral baseline fitting was an iterative process using the CASA task `imcontsub`. Almost all baselines were fit with zeroth order polynomials, with only a few exceptions requiring the use of first order polynomials. Visual inspections of the quality of the baseline removal for all spectral windows indicates good quality overall. For all but one spectral window, only 10 spectral channels are believed to be line-free (the Band 6 spectral window near 219 GHz is estimated to have 70 line-free channels). Following baseline subtraction the line-free channels from each spectral window were collapsed to form a pseudo-continuum image of NGC 253 in each spectral window. The properties of these pseudo-continuum images are listed in Table 3 and displayed in Figure 3. Note that the RMS noise values listed for these continuum images are in most cases slightly larger than a statistical averaging of the chosen individual line-free channels would suggest likely due to low-level line contamination and imaging artifacts.
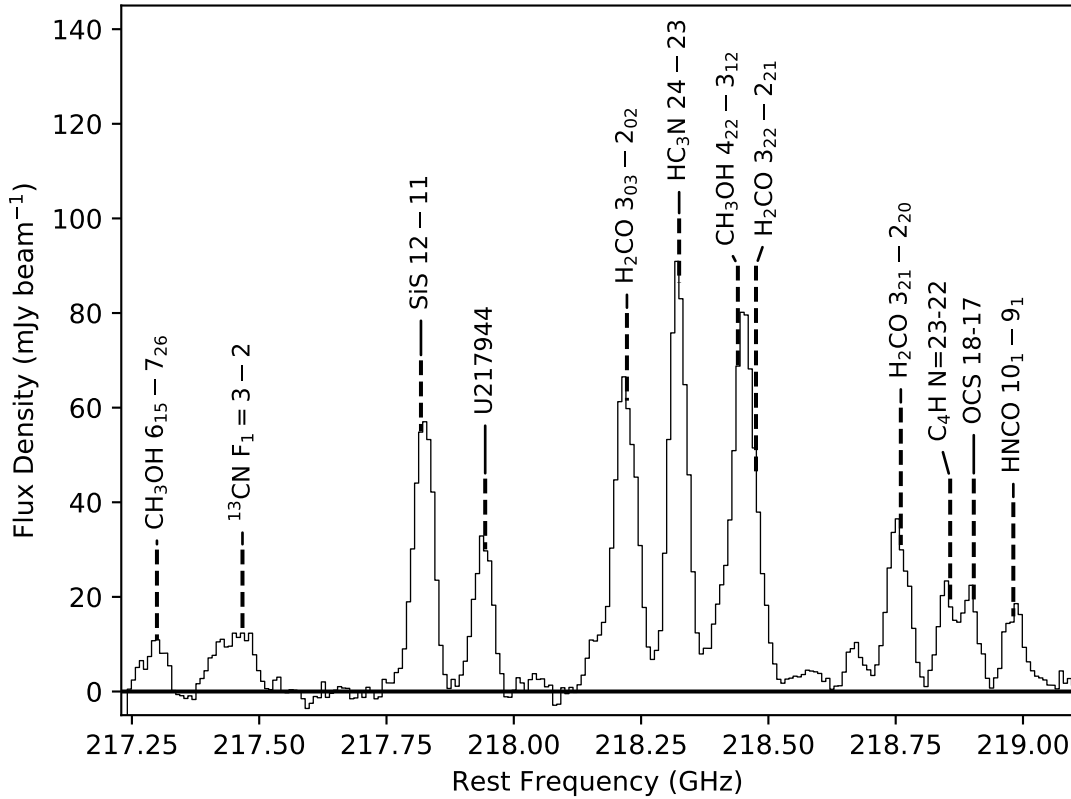
Figure 2. Sample spectrum from our NGC 253 Band 6 measurements centered at a rest frequency of 218.222192 GHz. Shown is the spectrum centered on Region 6 and averaged over a one arcsecond area and spectrally smoothed to 10 km/s. Identified molecular transitions are indicated.

As it will be convenient to interchange between flux and brightness temperature, we will use the general relation between the flux density of a source (S_ν) with solid angle Ω and its brightness temperature (T_B):

$$S_\nu = \frac{2k\nu^2}{c^2} \int T_B(\Omega) d\Omega \qquad (1)$$

Note that Equation 1 assumes that the Rayleigh-Jeans approximation ($h\nu \ll kT$) applies. Assuming $\int T_B d\Omega_s = T_B \Omega_s$ with Ω_s equal to the synthesized gaussian beam solid angle $\Omega_B = \frac{\pi \theta_{maj} \theta_{min}}{4 \ln 2}$ in Equation 1 results in the following general relation between flux density and measured brightness temperature for a point source:

$$T_B(K) \simeq 13.6 \left(\frac{300}{\nu(GHz)} \right)^2 \frac{S_\nu(Jy)}{\theta_{maj}(arcsec)\theta_{min}(arcsec)} \qquad (2)$$

3.2. Spatial Component Identification

Using the continuum images described in Section 3.1, we have fit single-component elliptical gaussians to each of the continuum peaks in these images. Table 4 lists the regions identified in our measurements, and also lists the corresponding components
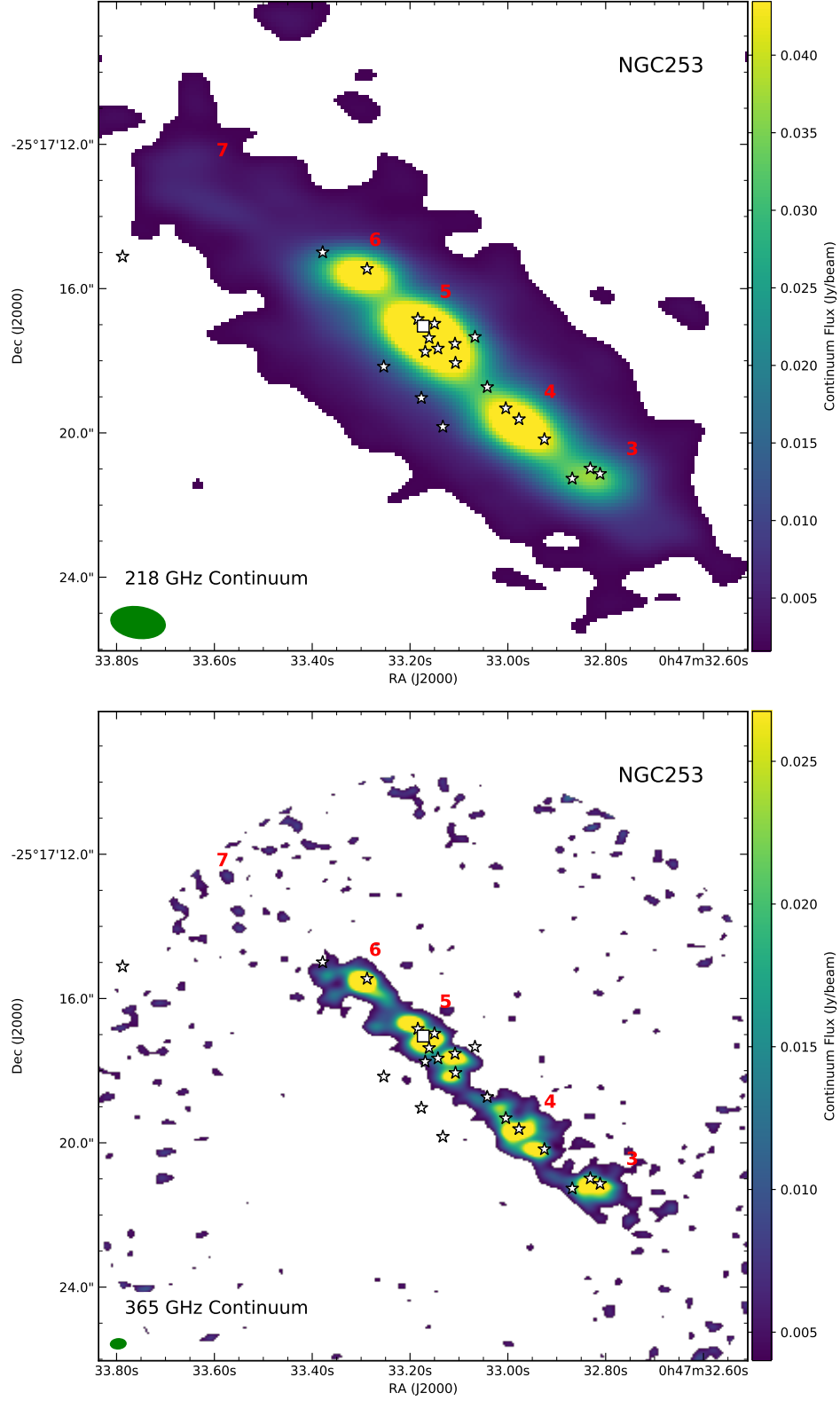
Figure 3. Band 6 (218 GHz with RMS = 0.8 mJy/beam; top) and Band 7 (365 GHz with RMS = 1.5 mJy/beam; bottom) continuum images of NGC 253, shown on the same spatial scale and range. Red numbers indicate the locations of the dense molecular emission regions identified by Leroy et al. (2015, Table 4). White black-bordered markers locate the positions of the 2 cm radio continuum emission peaks (Ulvestad & Antonucci 1997), with a square indicating the position of the strongest radio continuum peak identified by Turner & Ho (1985) (TH2: RA(J2000) = 00^h 47^m $33^s.18$, Dec(J2000) = $-25°$ $17'$ $16''.93$).

Table 4. NGC 253 Continuum Source Positions and Component Correspondence

Region[a]	RA(J2000)[b]	Dec(J2000)[b]	M2015[c]	S2011[c]	A2017[c]	TH1985[c]
	$(00^h\ 47^m)$	$(-25°\ 17')$				
3	$32.^s848$	$21.''05$	4	S1	8	9
4	$32.^s976$	$19.''79$	5	S2	$\cdots$	8
4a	$32.^s982$	$19.''70$	5 (subcomponent)	$\cdots$	6	8
4b	$32.^s950$	$20.''00$	5 (subcomponent)	$\cdots$	7	$\cdots$
5	$33.^s166$	$17.''29$	6	$\cdots$	$\cdots$	2–6
5a	$33.^s118$	$17.''63$	6 (subcomponent)	$\cdots$	4	6
5b	$33.^s129$	$17.''89$	6 (subcomponent)	$\cdots$	5	6
5c	$33.^s165$	$17.''18$	6 (subcomponent)	$\cdots$	2	2–5
5d	$33.^s196$	$16.''80$	6 (subcomponent)	$\cdots$	3	2
6	$33.^s297$	$15.''56$	7	S4	1	1
7	$33.^s637$	$13.''01$	8	S5	$\cdots$	$\cdots$

[a] Nomenclature adopts Leroy et al. (2015) component numbering.

[b] Position errors are all $< 0.25''$.

[c] M2015:Meier et al. (2015), S2011:Sakamoto et al. (2011), A2017:Ando et al. (2017), TH1985:Turner & Ho (1985).

noted by Leroy et al. (2015), Meier et al. (2015), Sakamoto et al. (2011), Ando et al. (2017), and Turner & Ho (1985). Note that components 4 and 5 split into multiple components in our higher-resolution Band 7 measurements, as previously noted by Ando et al. (2017). In the following we will use the regions noted in Table 4 as spatial reference positions for further analysis of the spectral emission properties within the nuclear disk of NGC 253.

3.3. *Spatial Component Hydrogen Column Density and Mass*

Using the peak continuum flux measurements derived from our spatial gaussian fits to our continuum images (Section 3.2), and assuming that the continuum emission is dominated by thermal dust emission, we have calculated the hydrogen column densities and masses using the well-worn dust emission assumptions elucidated by Hildebrand (1983). Assuming that the hydrogen column densities and masses are dominated by molecular hydrogen, the total column density and mass of hydrogen is given by:

$$N(H_2) \simeq 7.0 \times 10^{22} R_{gd} \left(\frac{\lambda(mm)}{0.4} \right)^{\beta} \frac{T_R(K)}{T_d(K)}\, cm^{-2} \tag{3}$$

$$M(H_2) \simeq 2 \times 10^{-4} R_{gd} \left(\frac{\lambda(mm)}{0.25} \right)^{\beta+3} D^2(kpc) S_\nu(Jy) \exp\left(\frac{14.4}{\lambda(mm) T_d(K)} - 1 \right) M_\odot \tag{4}$$

where we have assumed optically-thin dust emission ($T_R = T_d \left[1 - \exp(-\tau_\lambda)\right] \simeq T_d \tau_\lambda$) and parameterized the gas-to-dust mass ratio as R_{gd}. The assumption of optically-thin dust emission appears to be justified given the moderate continuum brightness temperatures of $\sim 0.5\,\mathrm{K}$ that we measure. This optically-thin assumption is also consistent with the submillimeter through infrared dust continuum measurements presented in Pérez-Beaupuits et al. (2018). The other variables are the wavelength of observation (λ) in millimeters, the dust emissivity power law (β), the radiation temperature corresponding to the measured continuum flux in Kelvin (T_R), and the dust temperature (T_d), also in Kelvin. We also use Equation 2 to convert our measured continuum fluxes (S_ν) to radiation temperatures (T_R) assuming the spatial resolutions associated with each continuum image. Assuming then that $R_{gd} = 150$, $\beta = 1.5$, and $T_d = 35\,\mathrm{K}$ (see discussion in Leroy et al. 2015, Section 3.1.1), with the associated region dust continuum fluxes, we derive the hydrogen column densities and masses listed in Table 5. The GMC hydrogen masses we derive are consistent with those measured by Leroy et al. (2015), and the sum of our GMC hydrogen masses is consistent with the total CMZ hydrogen mass of $4.5 \pm 1.3 \times 10^8\,\mathrm{M_\odot}$ measured by Pérez-Beaupuits et al. (2018).

Our assumption of $R_{gd} = 150$ follows that of Leroy et al. (2015) and Weiß et al. (2008), which leverages the elemental (carbon through nickel) depletion analysis presented in Draine (2011), which itself uses the Milky Way elemental depletion analysis presented in Jenkins (2009). The average depletion of all sightlines analyzed by Jenkins (2009) is $F_* = 0.36$, which implies a value for the gas-to-dust mass ratio of the diffuse Milky Way of $R_{gd} = 150$. Even though it is not clear if a diffuse gas Milky Way value for R_{gd} is appropriate to the dense CMZ of NGC 253, it is the only properly calibrated, through line-of-sight UV absorption measurements, value for this quantity.

In order to calculate molecular abundances using our total molecular column densities (Section 6), we average our GMC-specific hydrogen column densities per receiver band over any sub-components which comprise a main GMC in Table 5. These averaged hydrogen column densities (and masses) are listed in Table 6. As will be done for our calculations of the total molecular column density (Section 6), the uncertainties associated with each hydrogen column density and mass represent the larger of the statistical uncertainty and the standard deviation of the individual column densities or masses derived. These averaged hydrogen column densities will be used to derive molecular abundances within the GMCs of NGC 253.

4. ANALYSIS

4.1. Spectral Line Identification

Molecular spectral line identification within each spectral window of our NGC 253 measurements was done in two steps. In a first step the ALMA Data-Mining Toolkit (ADMIT; Teuben et al. 2015) was used to search for the most appropriate identification of spectral features based on the known velocity structure within the nucleus

Table 5. NGC 253 GMC Hydrogen Column Densities and Masses

Region[a]	S_ν (mJy)	$N(H_2)$ ($\times 10^{23}$ cm^{-2})[b]	$M(H_2)$ ($\times 10^6$ M$_\odot$)[b]
218 GHz Continuum; 1.52×0.87 arcsec			
3	31.07 ± 3.82	11.53 ± 1.42	12.11 ± 1.49
4	45.77 ± 4.48	16.99 ± 1.66	17.84 ± 1.75
5	68.24 ± 6.00	25.33 ± 2.23	26.60 ± 2.34
6	43.54 ± 5.52	16.16 ± 2.05	16.98 ± 2.15
7	4.64 ± 0.70	1.73 ± 0.26	1.82 ± 0.27
220 GHz Continuum; 1.56×0.89 arcsec			
3	25.96 ± 3.10	8.93 ± 1.07	9.80 ± 1.17
4	37.79 ± 3.54	13.00 ± 1.22	14.27 ± 1.34
5	54.71 ± 4.39	18.26 ± 1.51	20.65 ± 1.66
6	38.25 ± 4.18	13.16 ± 1.44	14.44 ± 1.58
7	2.48 ± 0.36	0.85 ± 0.12	0.93 ± 0.13
351 GHz Continuum; 0.45×0.29 arcsec			
3	38.66 ± 2.98	27.34 ± 2.10	2.11 ± 0.16
4a	42.41 ± 5.83	29.99 ± 4.12	2.32 ± 0.32
4b	60.98 ± 4.76	43.12 ± 3.37	3.33 ± 0.26
5a	25.99 ± 3.32	18.38 ± 2.35	1.42 ± 0.18
5b	41.54 ± 6.37	29.37 ± 4.51	2.27 ± 0.35
5c	48.15 ± 4.89	34.05 ± 3.46	2.63 ± 0.27
5d	52.51 ± 8.08	37.13 ± 5.71	2.87 ± 0.44
6	95.62 ± 7.31	67.62 ± 5.17	5.22 ± 0.40
7	2.74 ± 1.11	1.94 ± 0.79	0.15 ± 0.06
363 GHz Continuum; 0.43×0.28 arcsec			
3	40.21 ± 3.32	27.50 ± 2.27	1.93 ± 0.16
4a	45.27 ± 5.70	30.96 ± 3.90	2.17 ± 0.27
4b	65.97 ± 5.44	45.12 ± 3.72	3.16 ± 0.26
5a	28.32 ± 5.52	19.37 ± 3.78	1.36 ± 0.26
5b	46.02 ± 7.01	31.47 ± 4.79	2.21 ± 0.34
5c	51.79 ± 5.52	35.42 ± 3.78	2.48 ± 0.26
5d	56.16 ± 8.67	38.41 ± 5.93	2.69 ± 0.42
6	99.66 ± 7.85	68.16 ± 5.37	4.78 ± 0.38
7	4.57 ± 0.93	3.13 ± 0.64	0.22 ± 0.04
365 GHz Continuum; 0.43×0.28 arcsec			
3	40.41 ± 3.52	27.27 ± 2.38	1.91 ± 0.17
4a	45.54 ± 6.43	30.73 ± 4.34	2.15 ± 0.30
4b	66.44 ± 5.49	44.83 ± 3.70	3.14 ± 0.26
5a	29.94 ± 5.60	20.20 ± 3.78	1.41 ± 0.26
5b	43.96 ± 7.71	29.66 ± 5.20	2.08 ± 0.36
5c	53.62 ± 5.72	36.18 ± 3.86	2.53 ± 0.27
5d	59.93 ± 9.74	40.44 ± 6.57	2.83 ± 0.46
6	101.48 ± 7.99	68.48 ± 5.39	4.79 ± 0.38
7	4.15 ± 3.79	2.80 ± 2.56	0.20 ± 0.18

[a] Nomenclature adopts Leroy et al. (2015) component numbering.

[b] Assuming $R_{gd} = 150$, $T_d = 35$ K, $\tau_d \ll 1$, $\beta = 1.5$, and $D = 3.5$ Mpc.

Table 6. NGC 253 Average GMC Hydrogen Column Densities and Masses

Region[a]	$\langle N(H_2) \rangle$ ($\times 10^{23}$ cm^{-2})[b]	$\langle M(H_2) \rangle$ ($\times 10^6$ M$_\odot$)[b]
220 GHz Continuum; 1.5×0.9 arcsec		
3	10.23 ± 1.30	10.96 ± 1.15
4	15.00 ± 2.00	16.05 ± 1.79
5	21.80 ± 3.53	23.63 ± 2.98
6	14.66 ± 1.50	15.71 ± 1.33
7	1.29 ± 0.44	1.38 ± 0.44
360 GHz Continuum; 0.4×0.3 arcsec		
3	27.38 ± 1.31	1.98 ± 0.09
4	37.46 ± 6.93	2.71 ± 0.50
5	30.84 ± 7.38	2.23 ± 0.53
6	68.09 ± 3.06	4.93 ± 0.22
7	2.63 ± 0.92	0.19 ± 0.06

[a] Nomenclature adopts Leroy et al. (2015) component numbering.

[b] Assuming $R_{gd} = 150$, $T_d = 35$ K, $\tau_d \ll 1$, $\beta = 1.5$, and D $= 3.5$ Mpc.

of NGC 253. Once an initial set of molecular species was identified, residual species within each spectral window were identified by-eye using lists of line rest frequencies (Lovas 1992; Müller et al. 2001) and anticipated general abundances for potential species. Table 12 in Appendix B lists the molecular transitions and frequencies measured toward NGC 253.

The Band 6 low spectral resolution spectral window centered at a rest frequency of 234.7 GHz was anticipated to be line-free, and thus would have served as a sensitive continuum measurement. It was determined, though, that spectral lines existed in this spectral window with rest frequencies near 234.69 and 235.15 GHz. These spectral line frequencies are consistent with CH_3OH $4_2 - 5_1$ A at 234683.39 MHz and/or CH_3OH $5_{-4} - 6_{-3}$ E at 234698.45 MHz.

4.2. Spectral Line Signal Extraction and Spatial Component Fitting

In order to extract integrated spectral line intensities from our measurements we have developed a python script, called `CubeLineMoment`[2], which uses a series of spectral and spatial masks to extract integrated intensities for a defined list of target spectral frequencies. `CubeLineMoment` makes extensive use of `spectral-cube`[3].

The masking process begins by selecting a bright spectral line whose velocity structure is representative of the emission across the galaxy. Preferably, it should be

---

[2] https://github.com/keflavich/mangum_galaxies/blob/master/CubeLineMoment.py
[3] https://zenodo.org/record/1213217

maximally inclusive, such that all other lines emit over a smaller area in position-position-velocity (PPV) space, which here has right ascension, declination and helio-centric velocity as axes. Various images are computed based on this line, including noise, peak intensity, position of peak intensity, and second moment (velocity dispersion). The CO $2 - 1$ and H_2CO $5_{15} - 4_{14}$ transitions were found to be appropriate choices for the bright "tracer" transitions in our Band 6 and 7 spectral windows, respectively.

These maps are then converted into a PPV mask cube by producing Gaussian profiles at each spatial pixel with peak intensity, centroid, and width defined by the appropriate masks. The Gaussians are sampled onto the PPV grid defined by the target emission line. For each spatial pixel, spectral pixels are masked-out below the 1-σ level evaluated on the model Gaussian. By evaluating only on the model Gaussian, we exclude pixels above 1-σ at other parts of the spectrum, which otherwise would contribute significantly to the included region. The mask is then applied to the target emission line data cube, and moment 0, 1, and 2 maps are produced.

Integrated spectral line intensity images derived from our `CubeLineMoment` analysis are listed in Appendix C. In order to associate spectral line integrated intensities with each of the spatial components noted both in previous and the current measurements, we have used the `gaussfit_catalog`[4] application, which uses `pyspeckit`[5] to perform gaussian fits of the spatial molecular spectral line components associated with the regions listed in Table 4. As a characterization of the high-density component structure within the NGC 253 nucleus, and to provide an example of the spatial gaussian fits performed, Table 7 lists the derived averaged peak position and size for the nuclear regions derived from our H_2CO $3_{03} - 2_{02}$, $3_{21} - 2_{20}$, $5_{15} - 4_{14}$, $5_{05} - 4_{04}$, $5_{24} - 4_{23}$, $5_{23} - 4_{22}$, $5_3 - 4_3$ and $5_4 - 4_4$[6] integrated intensity images. We have compared the derived peak position for each H_2CO component to those which correspond to positions derived from our Band 6 and 7 dust continuum and the spectral line measurements of Leroy et al. (2015), Meier et al. (2015), Sakamoto et al. (2011), Ando et al. (2017), and Turner & Ho (1985) (Table 4). We find that with but one exception, all peak H_2CO positions are consistent within respective measurement uncertainties with their corresponding ALMA Band 6 and 7 continuum positions, and with component positions derived from the earlier works listed. For the one exception, Region 5, the H_2CO position differs by $(\Delta\mathrm{RA}, \Delta\mathrm{Dec}) = (+0.64, +0.69)\,\mathrm{arcsec}$ $((11, 12)\,\mathrm{pc})$ from its reference position. The position for Region 5 is derived from our Band 6 measurements, whose spatial resolution is $\theta_{maj} \times \theta_{min} \simeq 1.5 \times 0.9\,\mathrm{arcsec})$. Region 5 is also known to have substructure in higher-resolution measurements (including our Band 7 imaging), and has been suggested as a component which suffers from self-absorption in lower-excitation molecular spectral line measurements (Meier et al.

---

[4] https://github.com/radio-astro-tools/gaussfit_catalog
[5] https://pyspeckit.readthedocs.io/
[6] Since the $5_{33} - 4_{32}$ and $5_{32} - 4_{31}$ transition pair, and the $5_{42} - 4_{41}$ and $5_{41} - 4_{40}$ transition pair are both spectrally blended, we use the shorthand notation which drops the K_{+1} quantum number.

2015). Even though real molecular abundance gradients within Region 5 cannot be excluded, the currently most plausible explanation for this position shift between our H_2CO and dust continuum plus previous low-excitation molecular emission measurements is a complex emission structure below the spatial resolution and sensitivity of our measurements.

Table 7. Averaged Gaussian Fits to NGC 253 Formaldehyde Components

Region	RA(J2000) $(00^h\ 47^m)$	Dec(J2000) $(-25°\ 17')$	FWHM (arcsec,deg) $(\theta_{maj} \times \theta_{min}$ @ PA)
3	32.8258±0.0077	21.1676±0.0671	$1.19 \pm 0.78 \times 0.52 \pm 0.29$ @-59 ± 169
4	32.9644±0.0004	19.7354±0.0231	$1.90 \pm 0.14 \times 1.01 \pm 0.05$ @ 160 ± 11
4a	32.9833±0.0048	19.7554±0.1313	$0.61 \pm 0.30 \times 0.36 \pm 0.13$ @20 ± 38
4b	32.9537±0.0059	20.0595±0.1917	$0.85 \pm 0.37 \times 0.46 \pm 0.25$ @-38 ± 49
5	33.2129±0.0094	16.5954±0.0619	$2.89 \pm 0.20 \times 1.09 \pm 0.01$ @144 ± 0
5a	33.113±0.0014	17.6237±0.0173	$0.54 \pm 0.22 \times 0.26 \pm 0.05$ @-81 ± 84
5b	33.1298±0.0004	17.8931±0.0624	$0.51 \pm 0.15 \times 0.27 \pm 0.06$ @-49 ± 24
5c	33.1666±0.0044	17.2551±0.0819	$0.52 \pm 0.10 \times 0.38 \pm 0.07$ @-96 ± 151
5d	33.1979±0.0043	16.7585±0.0709	$0.68 \pm 0.34 \times 0.32 \pm 0.10$ @15 ± 70
6	33.2994±0.0063	15.5952±0.0869	$0.89 \pm 0.70 \times 0.54 \pm 0.32$ @39 ± 70
7	33.6378±0.0063	13.0969±0.1072	$0.88 \pm 0.46 \times 0.50 \pm 0.32$ @-78 ± 144

Table 8 lists the spectral line integrated intensities derived from the `CubeLineMoment` output and `gaussfit_catalog` gaussian fit analysis from all detected transitions which are not significantly blended and whose derived integrated intensity is larger than 2σ. Full-width half-maximum (FWHM) line widths derived from this analysis range from ~ 50 to $\sim 80\,km/s$ for most of our unblended spectral line measurements. Furthermore, these line widths show little variation over the Regions which comprise the NGC 253 CMZ. In the following sections we will use these integrated intensities to derive molecular column densities which we will subsequently use to study the kinetic temperature and molecular abundance ratios within the starburst nuclear components of NGC 253.

Table 8. NGC 253 Integrated Spectral Line Intensities (Jy km/s)[a]

Transition	Region 3	Region 4	Region 5	Region 6	Region 7
$^{13}CO\ 2-1$	16.15±4.11	19.51±4.00	(3.30)	26.53±4.55	11.92±3.20
$C^{18}O\ 2-1$	6.80±1.60	7.17±1.34	(1.07)	11.91±1.67	4.48±1.09
$^{13}CN,\ F_1=3\text{-}2$	(0.12)	1.42±0.17	(0.15)	1.29±0.13	(0.04)
SiS $12-11$	2.22±0.32	2.37±0.30	(0.29)	3.27±0.37	1.42±0.11
SO $6_5\text{-}5_4$	1.46±0.19	2.49±0.20	1.70±0.22	4.68±0.32	0.94±0.05
$SO_2\ 4_{22}-3_{13}$	1.05±0.11	0.94±0.10	0.54±0.09	1.32±0.15	0.20±0.07
$SO_2\ 5_{33}-4_{22}$	0.31±0.05	4a:0.25±0.06, 4b:0.66±0.12	5a:0.15±0.03, 5b:0.25±0.04, 5c:0.28±0.08, 5d:0.38±0.13	0.90±0.04	(0.04)
$SO_2\ 14_{4,10}-14_{3,11}$	0.21±0.07	4a:0.30±0.07, 4b:0.80±0.24	5a:0.37±0.10, 5b:(0.09), 5c:0.99±0.12, 5d:0.44±0.08	1.34±0.08	(0.03)
HNC $4-3$	3.90±0.81	4a:17.99±1.27, 4b:(1.61)	5a:6.03±2.22, 5b:3.62±2.16, 5c:6.05±1.47, 5d:(3.45)	28.77±1.38	1.54±0.22
HNC $4-3\ \nu_2=1f$	0.68±0.07	4a:1.81±0.07, 4b:(0.07)	5a:1.21±0.13, 5b:(0.17), 5c:(0.09), 5d:(0.56)	0.54±0.13	0.09±0.04

Table 8 continued on next page

Table 8 (continued)

Transition	Region 3	Region 4	Region 5	Region 6	Region 7
OCS $30-29$	1.30 ± 0.25	4a:2.55 ± 0.31, 4b:(0.38)	5a:1.08 ± 0.10, 5b:(0.78), 5c:2.97 ± 0.35, 5d:(0.46)	5.74 ± 0.68	0.71 ± 0.17
HNCO $10_0 - 9_0$[b]	4.58 ± 0.52	2.45 ± 0.32	(0.27)	4.70 ± 0.38	3.43 ± 0.20
HNCO $10_1 - 9_1$[b]	1.29 ± 0.12	0.82 ± 0.10	(0.14)	1.14 ± 0.09	0.18 ± 0.05
HNCO $10_2 - 9_2$[b]	$\cdots$	0.39 ± 0.04	(0.06)	0.55 ± 0.07	(0.03)
H$_2$CO $3_{03} - 2_{02}$	2.52 ± 0.37	2.99 ± 0.39	(0.35)	4.22 ± 0.49	2.96 ± 0.27
H$_2$CO $3_{21} - 2_{20}$	1.18 ± 0.19	2.01 ± 0.20	(0.19)	2.74 ± 0.20	1.20 ± 0.08
H$_2$CO $5_{05} - 4_{04}$[c]	$\cdots$	$\cdots$	$\cdots$	$\cdots$	$\cdots$
H$_2$CO $5_{24} - 4_{23}$	0.85 ± 0.08	4a:1.73 ± 0.10, 4b:0.50 ± 0.12	5a:0.91 ± 0.15, 5b:(0.16), 5c:0.45 ± 0.10, 5d:0.91 ± 0.34	3.83 ± 0.10	0.21 ± 0.07
H$_2$CO $5_{23} - 4_{22}$	0.46 ± 0.06	4a:1.41 ± 0.07, 4b:0.28 ± 0.09	5a:0.92 ± 0.10, 5b:(0.13), 5c:0.33 ± 0.09, 5d:0.60 ± 0.28	2.52 ± 0.11	0.64 ± 0.12
H$_2$CO $5_4 - 4_4$[d]	0.20 ± 0.04	4a:0.54 ± 0.06, 4b:0.34 ± 0.17	5a:0.35 ± 0.08, 5b:(0.12), 5c:0.56 ± 0.05, 5d:0.20 ± 0.10	(0.04)	(0.07)
H$_2$CO $5_{15} - 4_{14}$	1.73 ± 0.14	4a:3.74 ± 0.24, 4b:1.23 ± 0.28	5a:1.62 ± 0.29, 5b:1.26 ± 0.42, 5c:2.18 ± 0.30, 5d:1.80 ± 0.38	4.71 ± 0.42	0.63 ± 0.10

Table 8 (continued)

Transition	Region 3	Region 4	Region 5	Region 6	Region 7
H_2CO $5_3 - 4_3$[d]	1.29±0.11	4a:3.30±0.13, 4b:0.37±0.15	5a:1.75±0.32, 5b:(0.32), 5c:1.25±0.24, 5d:1.45±0.59	5.18±0.23	0.93±0.10
H_3O^+ $3_2 - 2_2$	1.08±0.23	4a:2.35±0.30, 4b:(0.37)	5a: ⋯ , 5b:0.64±0.58, 5c:2.63±0.33, 5d:1.09±0.41	5.46±0.68	0.65±0.15
HC_3N 24 – 23	2.38±0.27	2.85±0.27	2.66±0.35	6.63±0.54	1.29±0.10
HC_3N $24 - 23\nu_7 = 2$	(0.01)	0.06±0.02	2.44±0.39	0.55±0.14	0.09±0.04
HC_3N 40 – 39	0.77±0.07	4a:0.90±0.09, 4b:0.46±0.10	5a:0.52±0.14, 5b:(0.14), 5c:0.31±0.11, 5d:0.78±0.30	4.29±0.13	(0.13)
C_4H N=23-22[e]	0.36±0.06	0.51±0.05	0.56±0.09	1.71±0.10	0.045±0.03
CH_3CN 12 – 11	1.58±0.12	0.88±0.09	⋯	2.39±0.11	0.65±0.04
CH_3OH 9_5-10_4E	0.28±0.08	4a:0.25±0.14, 4b:1.09±0.03	5a:0.17±0.04, 5b:0.32±0.06, 5c:0.58±0.09, 5d:0.38±0.12	0.89±0.06	(0.03)
U217944[f]	1.17±0.15	⋯	⋯	2.10±0.20	0.47±0.06
U351047	0.96±0.13	4a:1.61±0.12, 4b: ⋯	5a:0.77±0.12, 5b:0.55±0.23, 5c:1.07±0.16, 5d:1.06±0.20	2.37±0.20	⋯

Table 8 *(continued)*

Transition	Region 3	Region 4	Region 5	Region 6	Region 7
U352199[f]	0.19±0.04	4a:0.36±0.04, 4b:(0.04)	5a:0.16±0.05, 5b:(0.04), 5c:0.36±0.05, 5d:0.24±0.08	0.87±0.04	···
U365185[f]	0.66±0.07	4a:1.84±0.07, 4b:(0.07)	5a:1.22±0.12, 5b:(0.17), 5c:0.20±0.09, 5d:0.91±0.59	7.41±0.12	···

[a] For values less than 2σ, RMS uncertainty listed in parentheses.

[b] All three HNCO transitions are blended with nearby species, making these HNCO integrated intensities uncertain.

[c] Blend with HNC $4-3$, making H_2CO integrated intensities unrecoverable.

[d] Since this is a blend of two transitions whose intensities should be equal, the measured intensity from Table 8 has been divided by 2 to calculate the column density.

[e] Composed of the blended (J=47/2-45/2,F=23-22), (J=47/2-45/2,F=24-23), (J=45/2-43/2,F=22-21), and (J=45/2-43/2,F=23-22) multiplet at 218837.00950 MHz.

[f] May be assigned as CH_3OCHO J=34-33 (U365185), CH_3OCHO $45_{14,32} - 45_{13,33}$ (U352199), and CH_3OCHO $45_{29,16} - 46_{28,18}$ (U217944)

5. KINETIC TEMPERATURE DERIVATION USING FORMALDEHYDE

As described by Mangum & Wootten (1993), the Formaldehyde molecule possesses structural properties which allow for its rotational transitions to be used as probes of the kinetic temperature in dense molecular gas environs. H_2CO is a slightly asymmetric rotor molecule, so that its energy levels are defined by three quantum numbers: total angular momentum J, the projection of J along the symmetry axis for a limiting prolate symmetric top, K_{-1}, and the projection of J along the symmetry axis for a limiting oblate symmetric top, K_{+1}. The H_2CO energy level diagram which shows all energy levels below $300\,K$ is shown in Figure 12 of Mangum & Wootten (1993).

For radiative excitation in a symmetric rotor molecule, dipole selection rules dictate that $\Delta K = 0$. Transitions between energy levels when $\Delta K \neq 0$ can only occur via collisional excitation. This, then, is the fundamental reason why symmetric rotor molecules are tracers of kinetic temperature in dense molecular clouds. A comparison between the energy level populations from different K-levels within the same molecular symmetry species (ortho or para) should allow a direct measure of the kinetic temperature in the gas. The asymmetry in H_2CO ($\kappa = -0.96$) makes it structurally similar to a prolate symmetric rotor molecule ($\kappa = -1.0$). Therefore, measurements of the relative intensities of two transitions whose K-levels originate from the same $\Delta J = 1$ transition provide a direct measure of the kinetic temperature.

To connect the kinetic temperature in the dense nuclear gas in starburst galaxies to the intensity of molecular transitions which originate from these nuclei, one needs to solve for the coupled statistical equilibrium and radiative transfer equations. A simple solution to these coupled equations is afforded by the Large Velocity Gradient (LVG) approximation (Sobolev 1960). The detailed properties of our implementation of the LVG approximation are described in Mangum & Wootten (1993). From the Mangum & Wootten (1993) summary of the uncertainties associated with LVG model results, we note that uncertainties in the collisional excitation rates (Green 1991), which can be as high as 50% for state-to-state rates, are not included in our analysis uncertainties. This contribution to the uncertainties of our derived physical conditions is traditionally ignored, and we only mention it here to provide context to our analysis. The simplified solution to the radiative transfer equation which the LVG approximation provides allows for a calculation of the global dense gas properties in a range of environments.

We have applied our LVG model formalism to the unblended H_2CO transitions measured toward NGC 253. With the nine transitions for which we have measured integrated intensities (Table 8) we can form five unique H_2CO transition ratios which can be used to derive the kinetic temperature in the dense nuclear regions of NGC 253. The analysis of the limits in kinetic temperature, volume density, and H_2CO column density to our measured H_2CO kinetic temperature sensitive ratios derived by Mangum & Wootten (1993) are directly applicable to our NGC 253 measurements. That analysis concluded that, over a volume density range of $n(H_2) = 10^{4.5} - 10^{8.5}\,cm^{-3}$

in a molecular cloud core, the following integrated intensity ratios measure kinetic temperature to an uncertainty of $\lesssim 25\,\%$:

- $\frac{Sdv(3_{03}-2_{02})}{Sdv(3_{21}-2_{20})}$ when $T_K \lesssim 50\,\mathrm{K}$ and $N(\text{para-H}_2\text{CO})/\Delta v \lesssim 10^{13.5}\,\mathrm{cm}^{-2}/(\mathrm{km\,s}^{-1})$. This rule also applies to the same ratio involving the $3_{22}-2_{21}$ transition.

- $\frac{Sdv(5_{05}-4_{04})}{Sdv(5_{23}-4_{22})}$ when $T_K \lesssim 75\,\mathrm{K}$ and $N(\text{para-H}_2\text{CO})/\Delta v \lesssim 10^{14.0}\,\mathrm{cm}^{-2}/(\mathrm{km\,s}^{-1})$. This rule also applies to the same ratio involving the $5_{24}-4_{23}$ transition.

- $\frac{Sdv(5_{24}-4_{23})}{Sdv(5_4-4_4)}$ when $T_K \lesssim 150\,\mathrm{K}$ and $N(\text{para-H}_2\text{CO})/\Delta v \lesssim 10^{14.5}\,\mathrm{cm}^{-2}/(\mathrm{km\,s}^{-1})$.

- $\frac{Sdv(5_{15}-4_{14})}{Sdv(5_3-4_3)}$ when $T_K \lesssim 100\,\mathrm{K}$ and $N(\text{ortho-H}_2\text{CO})/\Delta v \lesssim 10^{14.0}\,\mathrm{cm}^{-2}/(\mathrm{km\,s}^{-1})$

and to an upper limit, defined as the point at which the uncertainty in T_K becomes 50%, of:

- $T_K \lesssim 150\,\mathrm{K}$ for $\frac{Sdv(3_{03}-2_{02})}{Sdv(3_{21}-2_{20})}$. This rule also applies to the same ratio involving the $3_{22}-2_{21}$ transition.

- $T_K \lesssim 200\,\mathrm{K}$ $\frac{Sdv(5_{05}-4_{04})}{Sdv(5_{23}-4_{22})}$. This rule also applies to the same ratio involving the $5_{24}-4_{23}$ transition.

- $T_K \lesssim 300\,\mathrm{K}$ $\frac{Sdv(5_{24}-4_{23})}{Sdv(5_4-4_4)}$. This rule also applies to the same ratio involving the $5_{23}-4_{22}$ transition.

- $T_K \lesssim 250\,\mathrm{K}$ $\frac{Sdv(5_{15}-4_{14})}{Sdv(5_3-4_3)}$.

for the limits to the column densities per line width (FWZI) listed.

Due to velocity blending with the HNC $4-3$ transition the H_2CO $5_{05}-4_{04}$ transition cannot be used as a reliable kinetic temperature diagnostic in NGC 253. We rely then on the $\frac{Sdv(3_{03}-2_{02})}{Sdv(3_{21}-2_{20})}$, $\frac{Sdv(5_{15}-4_{14})}{Sdv(5_3-4_3)}$, $\frac{Sdv(5_{24}-4_{23})}{Sdv(5_4-4_4)}$, and $\frac{Sdv(5_{23}-4_{22})}{Sdv(5_4-4_4)}$ ratios to derive kinetic temperature images of the NGC 253 CMZ.

Over the range of H_2CO volume densities and kinetic temperatures appropriate to our NGC 253 measurements our measured kinetic temperature sensitive integrated intensity ratios are relatively insensitive to changes in H_2CO column density (Mangum & Wootten 1993). Therefore, we have interpolated our measured integrated intensity ratios onto our LVG model grid assuming $\log(N(species-H_2CO)/\Delta v) = 12.5\,\mathrm{cm}^{-2}/(\mathrm{km\ s}^{-1})$ and $\log(n(H_2)) = 5.0$ (Mangum et al. 2013a), where "species" is ortho or para. We have also applied the sensitivity limits listed above to properly identify the upper limit to the kinetic temperature sensitivity for each H_2CO transition ratio. This then allows us to convert our measured H_2CO integrated intensity ratios to kinetic temperatures. Figure 4 shows the results deduced from the above mentioned ratios and the resulting LVG model interpolation.

From our NGC 253 kinetic temperature images shown in Figure 4 we can conclude that:

- Based on the $\frac{Sdv(3_{03}-2_{02})}{Sdv(3_{21}-2_{20})}$ and $\frac{Sdv(5_{15}-4_{14})}{Sdv(5_3-4_3)}$ ratios the kinetic temperature ranges from 50 to $\gtrsim 150\,\mathrm{K}$ over dense gas regions as large as $\sim 5\,\mathrm{arcsec}$ ($\sim 80\,\mathrm{pc}$).
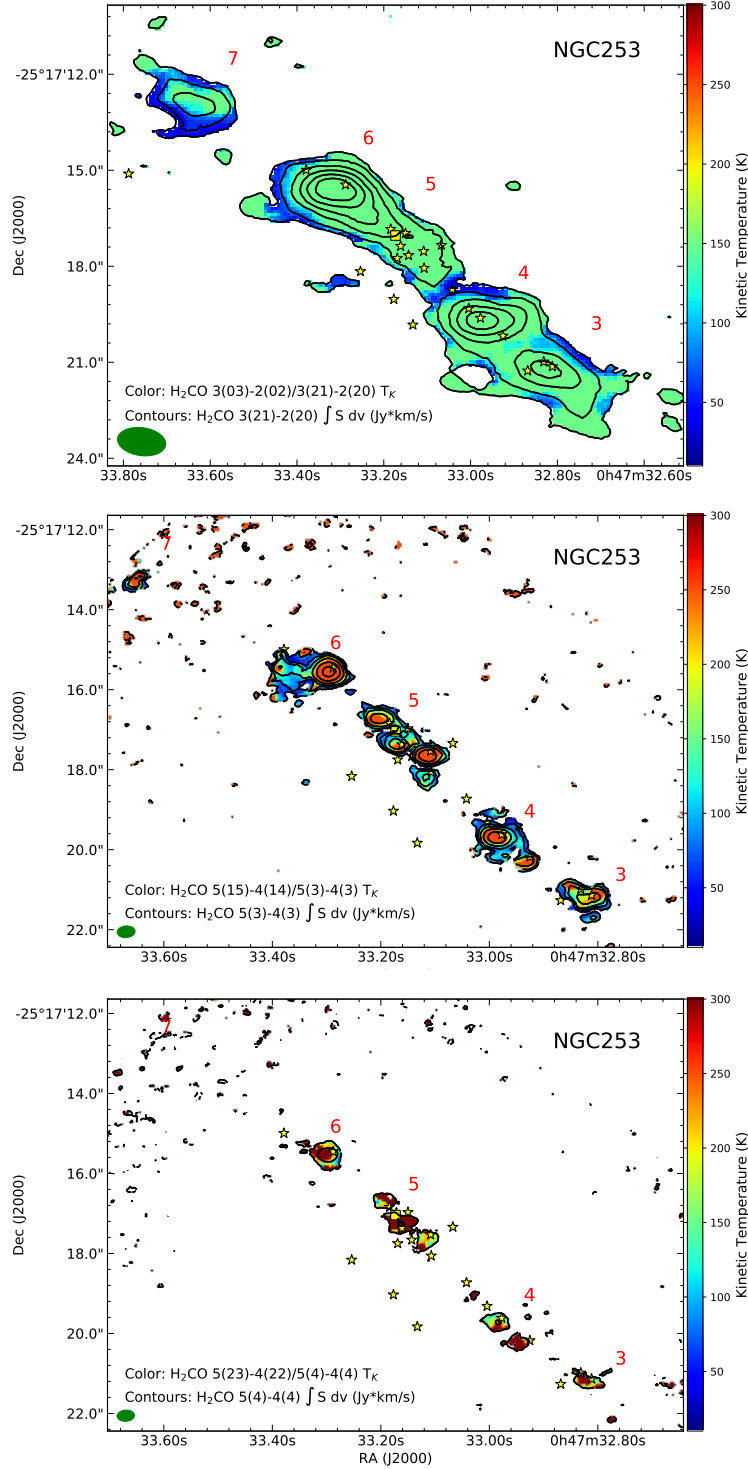
Figure 4. Kinetic temperature images derived from H_2CO integrated intensity ratios: $\frac{Sdv(3_{03}-2_{02})}{Sdv(3_{21}-2_{20})}$ (top), $\frac{Sdv(5_{15}-4_{14})}{Sdv(5_3-4_3)}$ (middle), $\frac{Sdv(5_{24}-4_{23})}{Sdv(5_4-4_4)}$ (bottom). Note that the appropriate upper sensitivity limit to the kinetic temperature scale has been applied based on the discussion in Section 5: 150 K (top), 250 K (middle), and 300 K (bottom). The synthesized beam is displayed in the lower-left of each panel. Red numbers indicate the locations of the dense molecular transition regions identified by Leroy et al. (2015, Table 4). Yellow stars locate the positions of the 2 cm radio continuum emission peaks (Ulvestad & Antonucci 1997), with a square indicating the position of the strongest radio continuum peak identified by Turner & Ho (1985) (TH2: RA(J2000) = $00^h\ 47^m\ 33^s.18$, Dec(J2000) = $-25°\ 17'\ 16''.93$). Contour levels are 0.25, 0.50, 1.0, 1.5, 2.0, and 2.5 Jy*km/s ($H_2CO\ 3_{21} - 2_{20}$); 0.10, 0.25, 0.50, 1.0, 2.0, and 4.0 Jy*km/s ($H_2CO\ 5_3 - 4_3$); and 0.10, 0.50 Jy*km/s ($H_2CO\ 5_4 - 4_4$).

- On smaller physical scales, $\lesssim 1\,$arcsec ($\lesssim 16\,$pc), our $\frac{Sdv(5_{15}-4_{14})}{Sdv(5_3-4_3)}$ and $\frac{Sdv(5_{24}-4_{23})}{Sdv(5_4-4_4)}$ ratios indicate that the kinetic temperature is greater than $300\,$K.

An analysis of the H_2CO $1_{10} - 1_{11}$ and $2_{11} - 2_{12}$ emission toward NGC 253 (Mangum et al. 2013a) measured volume densities $n(H_2) \geq 10^{4-5}\,cm^{-3}$. Furthermore, the effective critical density (Shirley 2015) for the H_2CO transitions considered in the current analysis is $n(H_2) \gtrsim 10^4\,cm^{-3}$. Our dense gas imaging of NGC 253 has therefore revealed volume densities that are greater than $10^{4-5}\,cm^{-3}$, our dense gas imaging of NGC 253 has revealed the existence of very high kinetic temperatures within the dense star-forming gas which encompasses a large area within the starburst nucleus of NGC 253. In Section 7 we will investigate the potential sources for these high dense gas kinetic temperatures.

5.1. *Comparison to Previous Kinetic Temperature Measurements*

As was summarized in Mangum et al. (2008), Mangum et al. (2013a), and Mangum et al. (2013b) numerous measurements of dense-gas molecular tracers have pointed to the existence of multiple temperature components in NGC 253. Three of the more recent studies of the nuclear kinetic temperature structure within NGC 253 (Mangum et al. 2013b; Gorski et al. 2017; Pérez-Beaupuits et al. 2018) suggest the existence of at least two kinetic temperature components:

- A warm component with $T_K \simeq 75\,$K

- A hot component with $T_K \gtrsim 150\,$K

A third cooler component with $T_K \simeq 40 - 50\,$K is also required by the dust and gas spectral energy distribution fits of Pérez-Beaupuits et al. (2018), though it may be difficult to distinguish this component from the cooler wings of a $75\,$K component in many of the previous high-excitation molecular spectral line measurements. These previous dense molecular gas kinetic temperature measurements are consistent with our H_2CO derived kinetic temperatures in NGC 253. The warm component measured in previous low spatial resolution studies is associated with dense gas on $\sim 80\,$pc scales, while the hot component appears to originate in dense gas on $\lesssim 16\,$pc scales.

6. MOLECULAR SPECTRAL LINE COLUMN DENSITY

In order to measure the relative abundances of the molecular species sampled by our ALMA imaging of NGC 253 we need to calculate the molecular column density for each species. In all but a handful of species we have sampled only one transition, which dictates that we perform a rather simplistic analysis of the molecular column density. With little information beyond the intensity and spatial distribution of each measured transition, to calculate molecular column densities we assume a kinetic temperature derived from our H_2CO measurements (see Section 5) in the optically-thin limit. With the additional assumptions that the excitation temperature of the measured position is much larger than the background temperature and equal to

the kinetic temperature, and that the source filling factor is unity, from Mangum & Shirley (2015) we adopt the total molecular column density in the optically-thin limit with $T_{ex} \gg T_{bg}$ given by:

$$N_{tot}^{thin} = \left(\frac{3k}{8\pi^3 S\mu^2\nu R_i} \right) \left(\frac{Q_{rot}}{g_J g_K g_I} \right) \exp\left(\frac{E_u}{T_K} \right) \int T_B dv \; cm^{-2}, \qquad (5)$$

where S is the transition line strength, μ is the molecular dipole moment in Debye, ν is the transition frequency in GHz, R_i is the relative transition intensity (for hyperfine transitions), g_J, g_I, and g_K are the rotational, nuclear spin, and K degeneracies, E_u is the transition upper energy level in Kelvin, T_K is the kinetic temperature in Kelvin, T_B is the measured transition brightness temperature, and Q_{rot} is the rotational partition function:

$$Q_{rot} = \sum_{J=0}^{\infty} \sum_{K=-J}^{J} g_K g_I (2J+1) \exp\left(-\frac{E_{JK}}{T_{rot}} \right) \qquad (6)$$

for linear (where the summation over K is removed), symmetric, and slightly-asymmetric rotor molecules. E_{JK} represents the energy above the ground state in Kelvin for a transition with quantum numbers (J,K). We assume that the rotational temperature, T_{rot}, is equal to the kinetic temperature. Inserting Equation 2 for T_B into Equation 5 results in the following:

$$N_{tot}^{thin} \simeq \frac{2.04 \times 10^{20} Q_{rot} \exp\left(\frac{E_u}{T_K} \right) \int S_\nu (Jy) dv(km/s)}{S\mu^2(Debye)\nu^3(GHz)R_i g_J g_K g_I \theta_{maj}(arcsec)\theta_{min}(arcsec)} \; cm^{-2} \qquad (7)$$

To check whether our assumption of optically-thin emission is reasonable, we compared our measured spectral line peak intensities to those derived from an LVG model prediction of those intensities. For example, our measured ^{13}CO and C^{18}O $3-2$ integrated intensities are $\sim 10-20$ Jy km/s (Table 8), with FWHM of ~ 50 km/s. For an LVG model which assumes $T_K = 150$ K (Section 5), n(H$_2$) $= 10^4 \, cm^{-3}$, and N(^{13}CO or C^{18}O) $= 10^{17}$ cm^{-2} (Table 9), we find that $\tau \simeq 0.1$ for both ^{13}CO and C^{18}O $3-2$, with predicted brightness temperatures similar to those that we measure. Furthermore, if one assumes a lower kinetic temperature of 50 K in these LVG calculations, τ increases modestly to $\simeq 0.3$. Similar estimates using LVG model calculations which use our measured peak brightness temperatures and column densities to estimate transition optical depths indicate that most of our measurements are well within the optically-thin regime, and only reach moderate optical depths in a few cases. Two such moderate optical depth cases are the H$_2$CO $3_{03} - 2_{02}$ and $3_{22} - 2_{21}$ transitions, for which $\tau \simeq 0.8$ and 0.4, respectively. As the H$_2$CO column density is based on a sample of seven transitions (Table 9), the moderate optical depths within these two transitions is unlikely to significantly affect the total H$_2$CO column density derived.

Using θ_{maj}, θ_{min}, and $\int S_\nu(Jy)dv(km/s)$ from Table 8 and the spectral line frequencies (ν), upper-state energies above ground (E_u), dipole moments (μ), line strengths

(S), transition degeneracies (g_J, g_K, g_I), and partition function values at representative kinetic temperatures ($Q_{rot}(T)$; Table 12), we calculate N_{tot}^{thin} in Table 9 using the indicated variable values and assuming $T_K = 150\,$K. We have chosen $T_K = 150\,$K as the representative kinetic temperature for our molecular column density calculations as it accounts for both the warm gas measured on GMC ($\sim 80\,$pc) spatial scales, and the hot gas measured on smaller ($\lesssim 16\,$pc) scales (see Section 5).

Note that to scale these total optically-thin molecular column densities to an assumed kinetic temperature other than $150\,$K, one simply needs to apply Equation 8 to the total molecular column densities listed in Table 9:

$$\frac{N_{tot}^{thin}(T_{K1})}{N_{tot}^{thin}(T_{K2})} = \frac{Q_{rot}(T_{K1})}{Q_{rot}(T_{K2})} \exp\left(\frac{E_u}{T_{K1}} - \frac{E_u}{T_{K2}}\right)$$
$$\simeq \left(\frac{T_{K1}}{T_{K2}}\right)^{\frac{n}{2}} \exp\left(\frac{E_u}{T_{K1}} - \frac{E_u}{T_{K2}}\right) \tag{8}$$

where we have used the fact that, to a very good approximation, $Q_{rot}(T_K) \propto T_K^{\frac{n}{2}}$, where $n = 2$ for linear molecules and $n = 3$ for symmetric and slightly-asymmetric rotor molecules (see Mangum & Shirley 2015, Section 7).

When multiple transitions are available (indicated by the N_{trans} column in Table 9), a spatially-averaged molecular column density is listed whose uncertainty is the larger of the statistical uncertainty and the standard deviation of the individual transition column densities derived. Spatial averaging is done in order to include measurements from both Bands 6 and 7, in that we have averaged over the Band 7 subcomponents within Regions 4 and 5. In Section 7.2 we will compare the relative abundances of the molecular species identified in our column density analysis with a goal of using these abundance ratios as a diagnostic of the heating processes in the NGC 253 starburst nuclear subcomponents.

Table 9. NGC 253 Component Total Molecular Column Densities[a]

Molecule	N_{trans}	$N_{tot}^{thin} \times 10^{14}\,\mathrm{cm}^{-2}$ at $T_K = 150$ K				
		Region 3	Region 4	Region 5	Region 6	Region 7
^{13}CO	1	$2.58 \pm 0.97(3)$	$2.70 \pm 1.07(3)$	(840)	$4.50 \pm 2.33(3)$	$2.21 \pm 0.80(3)$
C^{18}O	1	$1.15 \pm 0.48(3)$	$1.05 \pm 0.37(3)$	(288)	$2.37 \pm 0.68(3)$	$0.90 \pm 0.31(3)$
^{13}CN	1	(0.22)	2.29 ± 0.46	(0.28)	1.50 ± 0.23	(0.41)
SiS	1	2.61 ± 0.66	2.99 ± 0.67	(0.53)	3.71 ± 0.79	2.43 ± 0.31
SO	1	2.60 ± 0.64	6.68 ± 0.91	2.98 ± 0.70	12.71 ± 1.51	2.99 ± 0.28
SO$_2$	3	39.84 ± 6.12	27.47 ± 10.72	26.72 ± 9.68	112.23 ± 22.20	(4.50)
HNC	1	0.88 ± 0.41	5.84 ± 0.96	(4.27)	11.66 ± 0.97	0.34 ± 0.15
OCS	1	24.82 ± 8.57	(27.94)	104.62 ± 28.08	237.69 ± 50.83	(969.61)
HNCO	3	18.06 ± 6.54	7.04 ± 1.75	(1.25)	13.71 ± 4.55	10.94 ± 7.18
H$_2$CO	7	11.12 ± 5.11	38.04 ± 19.60	41.34 ± 10.28	47.11 ± 29.56	22.68 ± 5.14
H$_3$O$^+$	1	2.73 ± 1.02	(4.09)	13.26 ± 4.04	35.09 ± 8.30	(3.47)
HC$_3$N	2	1.26 ± 0.31	2.72 ± 1.26	2.23 ± 1.24	11.22 ± 7.38	0.89 ± 0.12
C$_4$H	1	0.07 ± 0.02	0.10 ± 0.02	0.05 ± 0.01	0.30 ± 0.03	(0.02)
CH$_3$CN[b]	1	(0.35)	(0.20)	$\cdots$	0.92 ± 0.36	0.41 ± 0.20
CH$_3$OH	1	(13.98)	(27.20)	(31.84)	87.08 ± 9.94	(73.57)

[a]Column density calculation includes both integrated intensity and gaussian fit uncertainties.

[b]Since the CH$_3$CN $12 - 11$ transition is a combination of the K=0 through 3 levels, the column density has been scaled by a factor of $\frac{72}{349}$ (using Sections 5 and 9 in Mangum & Shirley (2015)) to account for spin degeneracy and line strength differences.

7. WHAT DRIVES THE HIGH KINETIC TEMPERATURES IN NGC 253?

As was shown in Section 5 the kinetic temperature within the starburst nucleus of NGC 253 is ~ 50 to $\gtrsim 150\,\mathrm{K}$ on $\sim 80\,\mathrm{pc}$ scales, and rises to kinetic temperatures greater than $300\,\mathrm{K}$ on $\lesssim 16\,\mathrm{pc}$ scales. $\mathrm{NH_3}$ measurements yield similar values (Mangum et al. 2013b). Furthermore, note that the Galactic CMZ possesses similarly high kinetic temperatures over GMC ($\sim 80\,\mathrm{pc}$) size scales (Ginsburg et al. 2016; Ao et al. 2013). Mills & Morris (2013), from observations of high energy level $\mathrm{NH_3}$ absorption, find evidence for an even hotter gas component ($T_K > 350\,\mathrm{K}$) that is widespread in the Galactic CMZ. This component most likely originates in a lower density gas component that is not sampled by our $\mathrm{H_2CO}$ data, which exclusively trace dense gas. Our $T_K > 300\,\mathrm{K}$ gas thus *is not* a counterpart of the Galactic CMZ dilute gas component. What physical processes can maintain such high kinetic temperatures?

As we discussed previously in the context of the high dense gas kinetic temperatures measured using $\mathrm{NH_3}$ emission within a sample of starburst galaxies (Mangum et al. 2013b), high kinetic temperatures can be generated by cosmic ray (CR) and/or mechanical heating. CR heating can be effective at high column densities due to the small ($\sim 3 \times 10^{-26}\,\mathrm{cm^{-2}}$) $\mathrm{H_2}$ CR dissociation cross section (Pérez-Beaupuits et al. 2018). As noted in Mangum et al. (2013b), adapted chemical Photon Dominated Region (PDR) models have been used by a number of groups (e.g. Bayet et al. 2011; Meijerink et al. 2011) to study the effects of CR and mechanical heating on the chemical abundances within starburst galaxies. In these models, kinetic temperatures ranging up to $150\,\mathrm{K}$ can be generated by injecting varying amounts of CR and/or mechanical energy. For example, in the CR plus mechanical heating models of Meijerink et al. (2011), $\mathrm{T}_K \simeq 150\,\mathrm{K}$ is attained for a mechanical heating rate of $3 \times 10^{-18}\,\mathrm{erg\,cm^{-3}\,s^{-1}}$ in a high density ($\mathrm{n(H_2)} = 10^{5.5}\,\mathrm{cm^{-3}}$) high column density ($\mathrm{N(H_2)} > 10^{22}\,\mathrm{cm^{-2}}$) environment with CR rates ranging from $5 \times 10^{-17} - 5 \times 10^{-14}\,\mathrm{s^{-1}}$. In order to distinguish between different physical processes which can produce the signatures of CR and/or mechanical energy, in the following we evaluate the radiative and chemical diagnostics of energy input within starburst galaxies.

7.1. *Radio, Near-Infrared, and X-ray Diagnostics of Dense Gas Heating*

Radio wavelength measurements (Turner & Ho 1985; Ulvestad & Antonucci 1997; Brunthaler et al. 2009) ranging from $\lambda = 1.3$ to $20\,\mathrm{cm}$ have identified over 60 individual compact continuum sources within the NGC 253 central molecular zone. Figures 3 through 25 show the locations of the compact $2\,\mathrm{cm}$ continuum sources identified by Ulvestad & Antonucci (1997). The brightest of these radio continuum sources ($\mathrm{S(2\,cm)} \simeq 30\,\mathrm{mJy/beam}$ within $\theta \simeq 0.05\,\mathrm{arcsec}$) is located at the dynamical center of NGC 253 and has been suspected to be either a low-luminosity active galactic nucleus (LLAGN) or a compact supernova remnant (Turner & Ho 1985; Ulvestad & Antonucci 1997; Brunthaler et al. 2009). This nuclear continuum source (designated

"TH2" in this article and indicated by a filled-square in the figures presented) has a $\lambda = 2\,\text{cm}$ brightness temperature of $\gtrsim 4 \times 10^4\,\text{K}$ and a size $\lesssim 1\,\text{pc}$ (Turner & Ho 1985; Ulvestad & Antonucci 1997). This brightness temperature over such a compact region would suggest that the emission is due to synchrotron radiation from a LLAGN (Condon 1992). There are several additional observations, though, which argue against the LLAGN explanation for TH2:

- Over the 2 to 6 cm wavelength range the spectral index is $\alpha \simeq -0.2$ to -0.3 ($S_\nu \propto \nu^\alpha$; Turner & Ho 1985; Ulvestad & Antonucci 1997), which is more consistent with bremsstrahlung emission from HII regions than that from optically-thin synchrotron emission ($\alpha \simeq -0.75$).

- Brunthaler et al. (2009) failed to detect sub-parsec scale structure at 22 GHz toward TH2, suggesting that TH2 is a radio supernova or young supernova remnant.

- Even though Chandra X-ray observations of the nuclear region within NGC 253 (Weaver et al. 2002) suggest the presence of a LLAGN, the spatial resolution is not sufficient to distinguish between TH2 and TH4. The X-ray source detected by Chandra is in fact consistent with emission from ultra-luminous X-ray sources (i.e., x-ray binaries) in other galaxies (Brunthaler et al. 2009).

- Fernández-Ontiveros et al. (2009) found no IR or optical counterpart to TH2, suggesting that there is no AGN associated with TH2.

- Over an 8 year period Ulvestad & Antonucci (1997) monitored the stability of the fluxes of the compact continuum sources within NGC 253 at wavelengths from 20 to 1.3 cm. They found no compelling evidence for variability in any of the compact source fluxes, variability that one might expect to see from a LLAGN. This flux constancy timescale of 8-years also helps to constrain the radio supernova rate to $\lesssim 0.3\,\text{yr}^{-1}$, consistent with other estimates (e.g. Rieke et al. 1980, 1988).

Existing evidence suggests, then, that the radio wavelength emission from NGC 253 is dominated by that from HII regions, radio supernovae, and supernova remnants, and that the central source TH2 does not appear to contain a LLAGN.

Ulvestad & Antonucci (1997) classify the radio structure of the 2 cm continuum sources TH1, TH3, TH4, and TH6 as structurally resolved with spectral indices α in the 1.3 to 6 cm wavelength range of ~ -0.5 to $+0.35$. Each of these radio continuum sources is associated with the dense-gas GMC Regions 6, 5c, 5c, and 5a/5b, respectively. These sources have 2 cm fluxes of 4 to 13 mJy (Ulvestad & Antonucci 1997), and are prototypes of what appear to be HII regions ionized by hot young stars. Analyzing just the radio emission properties of TH6, Ulvestad & Antonucci (1997) calculate that there are at least 5.2×10^{51} ionizing photons per second produced from a region $\sim 0.2 \times 0.1\,\text{arsec}$ in size. This ionizing photon flux is equivalent

to the emission produced by ~ 100 O5 stars in this HII region, and corresponds to the upper-end of the incident UV fields modeled by Meijerink et al. (2011); $10^5 G_0$, where $G_0 = 1.6 \times 10^{-3} \, \mathrm{erg \, cm^{-2} \, s^{-1}}$ (= one Habing). This would make TH6 a slightly more powerful version of the R136 cluster in the 30 Doradus region in the Large Magellanic Cloud (Kalari et al. 2018).

Further evidence for a variety of heating processes is provided by near-infrared diagnostic probes such as Brγ, H$_2$, and [FeII]. Rosenberg et al. (2013) imaged the Brγ, H$_2$, and [FeII] emission toward NGC 253, finding that all three trace the CMZ of NGC 253, but with variations in intensity that suggest dominance of specific heating processes within specific regions of the NGC 253 CMZ. An example of the correlation between the millimeter continuum (dust) emission distribution from our Band 7 measurements and the Brγ emission imaged by Rosenberg et al. (2013) is shown in Figure 5. Brγ traces the emission from young massive stars, and peaks near Region 4 in the dust and molecular emission. This region also corresponds to the "Infrared Core", a region which dominates the emission at infrared wavelengths (see Section 8). The [FeII] emission, on the other hand, is stronger toward Regions 5, 6, and 7. As [FeII] is a tracer of strong, grain destroying, shocks ($\mathrm{v}_{shock} \gtrsim 25 \, \mathrm{km/s}$, the [FeII] distribution suggests that shock heating is more prevalent toward Regions 5, 6, and 7. It seems clear from these examples that active massive star formation can provide the energy necessary to heat the dense gas in the nucleus of NGC 253 through a variety of physical processes.

7.2. *Chemical Diagnostics of Dense Gas Heating*

In order to compare our molecular spectral line measurements of the GMCs of NGC 253 with molecular abundance predictions from galactic starburst chemical models, we need to calculate the measured molecular abundances ($X(mol) \equiv \frac{N_{tot}^{thin}(mol)}{N(H_2)}$) using the total hydrogen and molecular column densities listed in Tables 6 and 9. Table 10 lists these calculated abundances, which are displayed in Figure 6. Recall that in the calculations of the hydrogen column density and mass presented in this section we have adopted the dust temperature assumed by Leroy et al. (2015); $\mathrm{T}_d = 35 \, \mathrm{K}$.

Some trends in our measured molecular abundances are apparent in Figure 6:

- For ^{13}CN, SiS, SO, SO$_2$, HNCO, HC$_3$N, and C$_4$H, Region 5, the Region associated with the central source, TH2, possesses the lowest abundance of the five Regions studied.

- For SiS, SO, HNCO, and HC$_3$N, in addition to Region 5 possessing the lowest abundance, Region 7, the region studied in this work which is the farthest from the NGC 253 nucleus, possesses the highest abundance.

- For those molecular species common to both studies, our derived molecular abundances are within the same range of 5×10^{-9} to 5×10^{-10} as those derived by Martín et al. (2006).
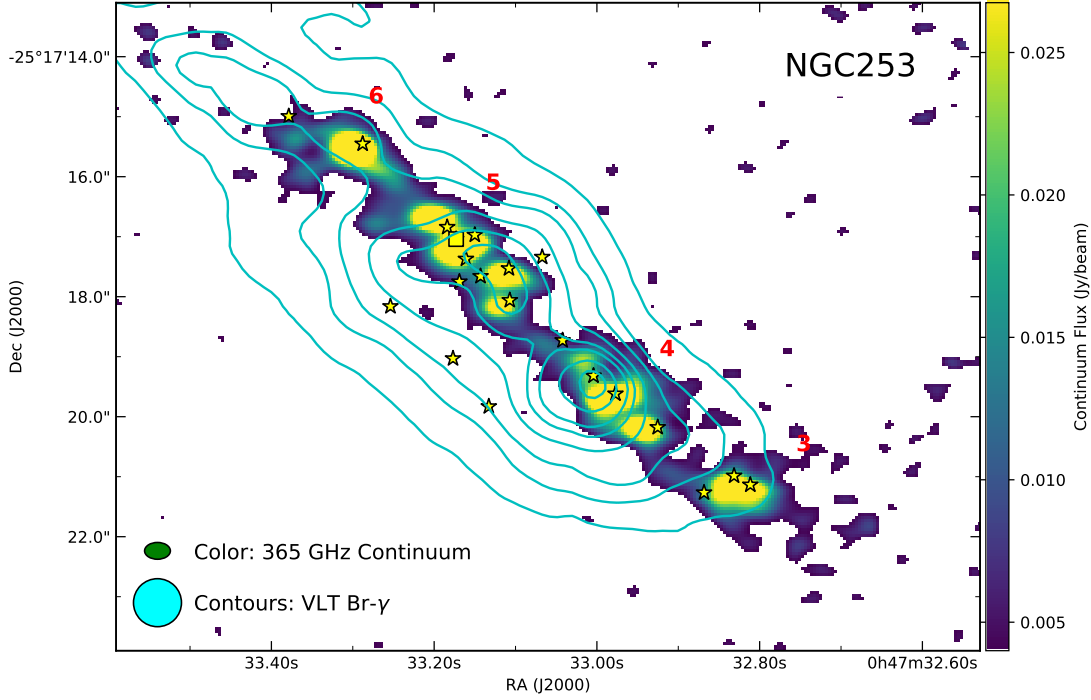
Figure 5. Comparison of the 365 GHz continuum (color) and VLT Brγ (contours; Rosen-berg et al. 2013) emission distributions toward the CMZ of NGC 253. Contour levels are 0.2, 0.4, 0.6, 1.0, 1.5, 2.0, 3.0, and 4.0 ×10^{-13} erg cm^{-2} s^{-1} arcsec^{-2}. The spatial resolution for both images is shown in the lower-left corner. Red numbers indicate the locations of the dense molecular transition regions identified by Leroy et al. (2015, Table 4). Note that we have adopted the astronometry from Fernández-Ontiveros et al. (2009) to define the absolute positions in the Brγ image.

These molecular abundance patterns could be related to the spatial distribution of energy sources, such as sources of cosmic rays and mechanical energy, within the NGC 253 CMZ. Past surveys designed to sample the dominant chemical processes in NGC 253 (e.g. Martín et al. 2006; Aladro et al. 2015) have noted the influence of the burst of star formation on the energetics within NGC 253. To tease-out the relative dominance of different dense gas heating processes, models which predict the varia-tion in molecular abundances within starburst environments have been developed. In general, these models characterize the changes in molecular abundances as a function of metallicity (z), volume density (n(H$_2$)), radiation field intensity (G$_0$), cosmic ray rate (ζ), and mechanical heating (Γ$_{mech}$). These physical processes are then coupled to chemical model networks to allow for the prediction of molecular abundances as a function of varying physical conditions. These molecular abundance predictions can then be used to guide our understanding of the abundance distributions measured in Galactic and extragalactic star formation regions. The adapted chemical-PDR mod-els of Meijerink et al. (2011) and Bayet et al. (2011) are of this type, and have been

Table 10. NGC 253 Component Total Molecular Abundances[a]

Molecule	X_{tot}(Molecule) $\times 10^{-10}$				
	Region 3	Region 4	Region 5	Region 6	Region 7
^{13}CN	(0.65)	1.53 ± 0.37	(0.38)	1.02 ± 0.19	(9.53)
SiS	2.55 ± 0.72	1.99 ± 0.52	(0.73)	2.53 ± 0.60	18.84 ± 6.86
SO	2.54 ± 0.70	4.45 ± 0.85	1.37 ± 0.39	8.67 ± 1.36	23.18 ± 8.20
SO$_2$	38.94 ± 7.76	18.31 ± 7.56	12.26 ± 4.86	76.55 ± 17.05	(104.65)
HNC	0.86 ± 0.42	3.89 ± 0.82	(5.88)	7.95 ± 1.05	2.64 ± 1.47
OCS	24.26 ± 8.93	(55.88)	47.99 ± 15.04	162.14 ± 38.44	(22549.07)
HNCO	17.65 ± 6.78	4.69 ± 1.32	1.72 ± 0.64	9.35 ± 3.25	84.81 ± 62.73
H$_2$CO	10.87 ± 5.18	25.36 ± 13.50	18.96 ± 5.63	32.14 ± 20.43	175.81 ± 72.00
H$_3$O$^+$	2.67 ± 1.05	8.18 ± 2.94	6.08 ± 2.10	23.94 ± 6.17	(80.70)
HC$_3$N	1.23 ± 0.34	1.81 ± 0.87	1.02 ± 0.59	7.65 ± 5.09	6.90 ± 2.53
C$_4$H	0.07 ± 0.02	0.07 ± 0.02	0.02 ± 0.006	0.20 ± 0.03	(0.47)
CH$_3$CN	(1.03)	(0.4)	. . .	0.63 ± 0.25	3.18 ± 1.89
CH$_3$OH	(41.00)	(54.40)	(43.82)	59.40 ± 9.11	(1710.93)

[a]Derived from measured total optically-thin molecular abundances (Table 9) and dust-continuum derived H$_2$ column densities (Table 6). Upper limits, listed in parentheses, are quoted as 3σ.

specifically designed to predict molecular abundances in extreme star formation environments such as starburst galaxies and very high star formation-rate ultra luminous infrared galaxies (U)LIRGs. Even though these two models have been used to predict molecular abundances within somewhat different sets of physical conditions, in general these models predict that when the cosmic ray ionization rate ζ is increased, the abundances of molecular species other than simple ions such as OH$^+$, CO$^+$, CH$^+$, and H$_2$O$^+$ (none of which are part of this study) decrease. The range of ζ modeled in these studies runs from the canonical Milky Way value of $2.6 \pm 0.8 \times 10^{-17}$ s^{-1} (van der Tak & van Dishoeck 2000) to 5×10^{-13} s^{-1}. This upper limit to ζ is roughly ten-times the cosmic ray ionization rate determined for NGC 253 from ultra-high energy cosmic ray observations, which is $\zeta \simeq 3.6 \times 10^{-14}$ s^{-1} (Acero et al. 2009), and is believed to be consistent with cosmic ray densities in ULIRGs (Papadopoulos 2010). The supernova rate which corresponds to the measured gamma-ray flux from NGC 253 is ~ 0.1 yr^{-1} (Acero et al. 2009), which is most pronounced towards its nucleus[7].

Given the existence of strong IR radiation fields in the NGC 253 CMZ, a note of caution is in order regarding the interpretation of rotational transition intensities for molecules which might be affected by radiative pumping of vibrational states that subsequently experience radiative decay. HCN, HNC and HC$_3$N (Section 8) show vibrationally-excited emission in NGC 253. Rotational energy levels in other

---

[7] Note, though, that the H. E. S. S. measurements from which the gamma-ray flux is derived have a spatial resolution of ~ 4.2 arcmin.
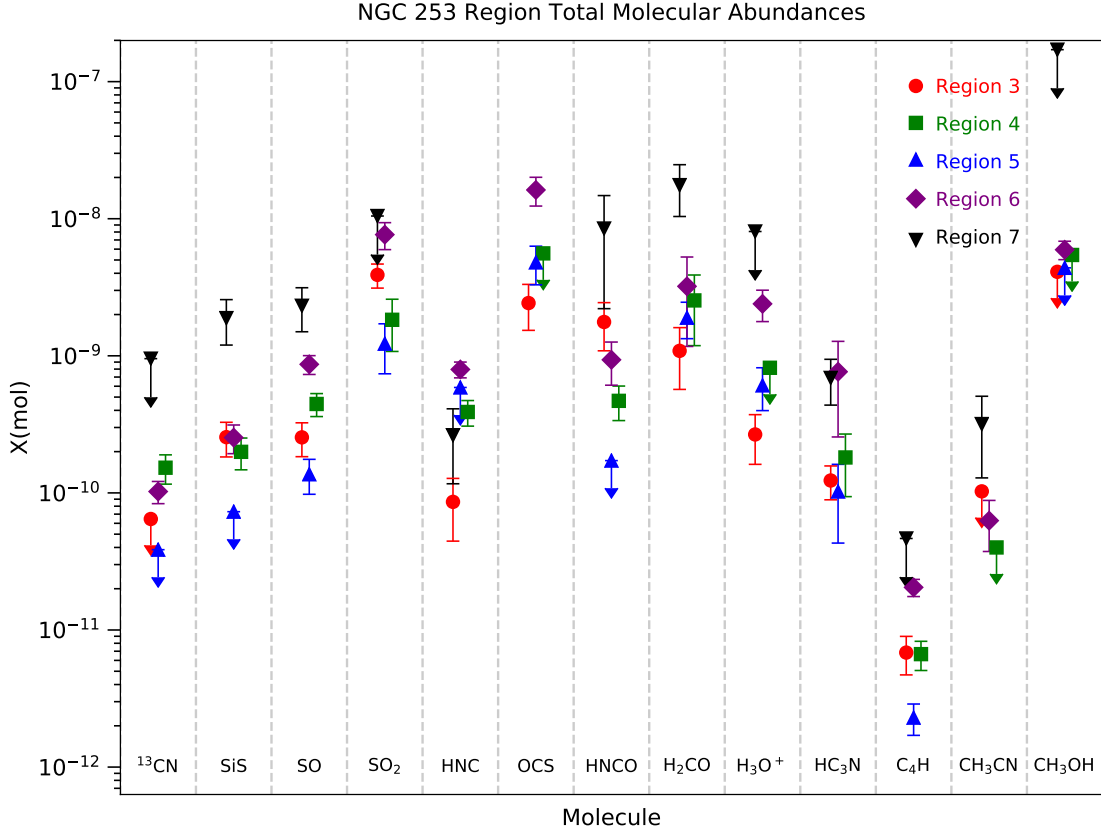
**Figure 6.** Total molecular abundances, excluding ^{13}CO and C^{18}O, derived from the total molecular column densities listed in Table 9. Limits are shown with downward arrows.

molecules, including H$_2$CO (Mangum & Wootten 1993), can also be excited by far-infrared emission, representing a potential unaccounted source of excitation of these molecules. Physical scenarios which attempt to describe infrared excitation of molecular rotational energy levels in molecules (Carroll & Goldsmith 1981; Mangum & Wootten 1993) tend to require that the sources of infrared emission be cospatial with the molecular distribution. Our measurements of vibrationally-excited HNC and HC$_3$N emission (Section 8) suggest that this emission could possess similar spatial distributions to their rotationally-excited counterparts. We would expect that if infrared excitation through vibrational transitions was signficantly contributing to the purely rotationally-excited transitions that we measure, we would expect to see local maxima in their spatial distributions which correspond to peaks in the vibrationally-excited emission from a given molecule. We have found that Region 6 represents a local maximum in vibrationally-excited HNC and HC$_3$N emission (Section 8), suggesting caution when interpreting the rotationally-excited emission from these molecules toward Region 6.

Comparing our molecular abundance measurements to the model predictions of Meijerink et al. (2011) and Bayet et al. (2011):

- Bayet et al. (2011) and Meijerink et al. (2011) modeled H_3O^+ and found that its abundance maintains a high level (of about 10^{-9} to 10^{-8}, respectively) under a wide range of conditions, peaking at CR rates of $\sim 10^{-15}$ to $10^{-13}\,s^{-1}$ at solar metallicity when the H_2 column density becomes high. Our measured abundance of H_3O^+ ($\sim 10^{-9}$) seems to be consistent with both the Bayet and Meijerink predictions.

- Bayet et al. (2011) modeled SO and found that it is destroyed by cosmic rays starting at $10^{-16}\,s^{-1}$. The Regional SO abundance pattern we measure, with Region 5 showing the lowest abundance and Region 7 showing the highest, seems to be consistent with a higher concentration of cosmic rays at the center of the NGC 253 CMZ than in its outskirts.

- As H_3O^+ abundances are enhanced by CRs, while SO is destroyed by CRs, we have made a direct comparison of the abundances of these two direct CR tracers for the different regions (Figure 7). Region 5 has an H_3O^+/SO abundance ratio more than 30% larger than that in Regions 3, 4, 6, and 7, suggestive of enhanced CR heating near the center of NGC 253. Note, though, that this abundance ratio assumes optically-thin emission from both molecules. Variations in the relative optical depth within the transitions measured to calculate this abundance ratio could at least partially explain this difference. Furthermore, our H_3O^+ and SO measurements were made with different tunings of the ALMA receiver system, making their abundance ratio susceptible to our estimated absolute amplitude calibration uncertainties of 10% and 15% at Bands 6 and 7, respectively (Appendix A). Factor of two differences could be explained by these two effects.

- Meijerink et al. (2011) noted no obvious trends in HNC abundance as a function of cosmic ray rates. We see no significant variation in X(HNC) amongst the various regions.

- The abundance of H_2CO has been modeled by Bayet et al. (2011) and Meijerink et al. (2011). The changes in H_2CO abundance predicted by these models is largely consistent with those of other complex molecules, and with our measurements. H_2CO is destroyed by cosmic rays at low densities.

- Meier & Turner (2012) investigated shock chemistry influence on CH_3OH, HNCO, and SiO abundances. They noted that CH_3OH and HNCO are possibly formed on grain mantles, so simply require enough energy to liberate them into the gas phase. This can be done with a shock which has $10 \lesssim v_{shock} \lesssim 15\,km/s$ (grain destruction happens for $v_{shock} \gtrsim 25\,km/s$). Meier & Turner (2012) also
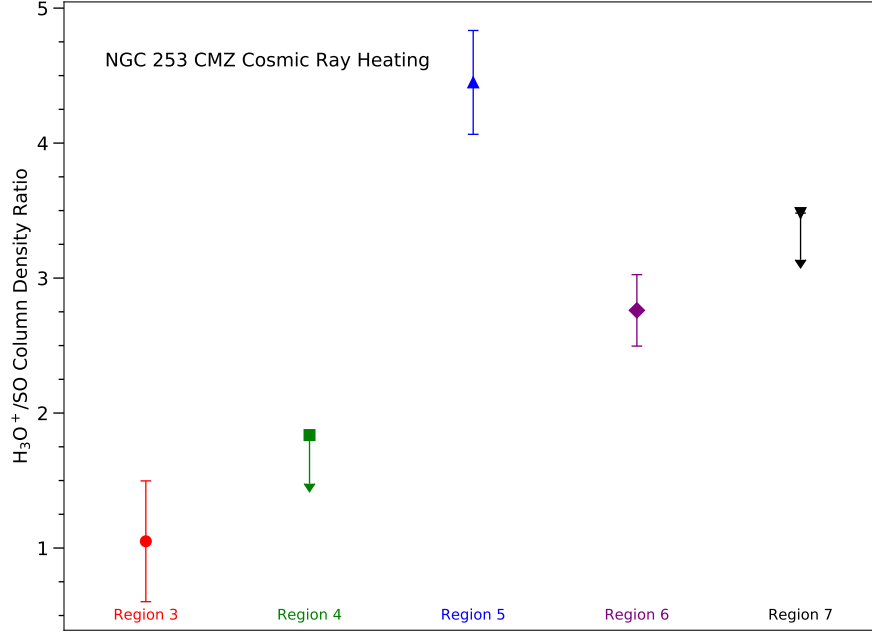
Figure 7. Total H_3O^+/SO abundance ratio for each region in the NGC 253 CMZ. Derived from the total molecular column densities listed in Table 9. Limits, shown with down arrows, have been calculated assuming three times the RMS of the undetected H_3O^+ column density.

noted that the photodissociation rate for HNCO is twice that for CH_3OH and ~ 30 times that of SiO. There are also large numbers of HII regions in Region 5 (Ulvestad & Antonucci 1997). Leroy et al. (2018), referring to the Gorski et al. (2017, 2018) imaging of the relatively-unattenuated $\sim 36\,GHz$ free-free emission from the GMCs in NGC 253, have noted the utility of these continuum measurements as a sensitive measure of the free-free emission from young heavily-embedded massive stars in NGC 253. Region 5 is the most intense source of $\sim 36\,GHz$ continuum emission in the NGC 253 CMZ. These embedded HII regions could explain our nondetection of HNCO in Region 5.

- Note also that cosmic rays are toxic to many molecules (Bayet et al. 2011; Meijerink et al. 2011), where abundances of molecules such as e.g.CN, SO, HNC, HCN, OCS, and H_2CO are shown to decrease by upwards of 10^3 when the CR rate increases from 10^{-16} to $10^{-14}\,s^{-1}$. Low abundances of many molecules in Region 5 might be due to a higher cosmic ray rate in this Region.

- Region 7 is the farthest away from the main source of cosmic rays. Its higher level of complex molecular abundances relative to regions closer to the center of the galaxy is consistent with a lower level of cosmic ray heating.

To identify possible sources of cosmic rays, we note that Ulvestad & Antonucci (1997) calculated spectral indices for all of the radio sources they detected. In those measurements spectral indices in the range $\alpha < -0.4$ are more common in the Region 5 area (where TH2 through TH6 are located) than elsewhere in the NGC 253 CMZ. Since spectral indices in this range would imply synchrotron emission, which can be generated by supernova remnants, and which produce cosmic rays, one might expect a larger flux of cosmic rays in Region 5 than within the other Regions. Cosmic ray heating, then, appears to be a plausible mechanism by which the GMCs in the CMZ of NGC 253 are heated to the high kinetic temperatures that we measure. Variations in the molecular abundances in these GMCs support this cosmic ray heating dominated scenario, but also do not rule out a significant influence due to mechanical heating.

The recent dust and molecular spectral line study of the ~ 40 arcsec-scale structures within the NGC 253 CMZ by Pérez-Beaupuits et al. (2018) concludes that mechanical heating is responsible for the highest kinetic temperatures measured within NGC 253. Analysis of the submillimeter dust and CO spectral energy distributions (SEDs) indicates that mechanical heating drives the high kinetic temperatures for the higher-excitation ($J_u > 13$) CO transitions, but not the lower-excitation transitions. Pérez-Beaupuits et al. (2018) note also that the effects and role of CRs in the dense gas heating process within the NGC 253 CMZ cannot be assessed through their measurements.

While we conclude that CRs may be responsible for the high observed temperatures in NGC 253's CMZ, Ginsburg et al. (2016) reached a somewhat different conclusion for the Milky Way's CMZ. Their inference was based on the mismatch between dust and gas temperature at moderately high density ($\sim 10^{4-5}$), which is difficult to explain by cosmic ray heating and is better explained by mechanical (turbulent) heating. Ginsburg et al. (2016) notably found no regional variance, instead finding that the elevated T_{gas}/T_{dust} was relatively uniform across the CMZ. By contrast, we have found that there are significant regional variations in molecular abundances and that these variations are correlated with the locations of likely supernova remnants. It therefore seems that the temperature structure in NGC 253 is more heavily influenced by CRs than the Milky Way CMZ because of its higher star formation (and therefore supernova) rate.

8. VIBRATIONALLY-EXCITED MOLECULES AND POSSIBLE NON-LTE METHANOL EMISSION

The molecular emission from vibrationally-excited HC$_3$N $24 - 23$ $\nu_7 = 2$ and HNC $4-3$ $\nu_2 = 1f$ transitions at 219675.114 and 365147.495 GHz, respectively, are detected toward Regions 3 through 7 (see Figure 8). With the exception of Region 3 in the HC$_3$N $24 - 23$ $\nu_7 = 2$ transition, vibrationally-excited integrated intensities are at greater than twice the integrated intensity RMS noise levels in our measurements. Contrary to the integrated emission from transitions within the vibrational ground

states of the molecules we study, though, the spatial distribution for HC_3N $24-23$ $\nu_7 = 2$ and HNC $4-3$ $\nu_2 = 1f$ is strongly peaked toward Region 6. As noted by Ando et al. (2017), who also reported the detection of HNC $4-3$ $\nu_2 = 1f$, this is the third detection of vibrationally-excited HNC toward an external galaxy, the others being the Luminous Infrared Galaxies (LIRGs) NGC 4418 (Costagliola et al. 2013, 2015) and IRAS 20551−4250 (Imanishi et al. 2016).

A similar spatial distribution is measured from the CH_3OH $9_5 - 10_4E$ transition at 351.236 GHz (Figure 8) and the CH_3OH $13_0 - 12_1A^+$ transition near 355.6 GHz (Ando et al. 2017). For both transitions the strongest emission emanates from Region 6. For reference, the 36.2 GHz $4_{-1} - 3_0E$ CH_3OH maser emission sources in NGC 253 (Ellingsen et al. 2014; Chen et al. 2018) emanate from Leroy et al. (2015) Regions 1, 7, and 8, on the far edges of the CMZ imaged in our measurements. Region 1 is also the source of HC_3N $4-3$ maser emission (Ellingsen et al. 2017). As the emission distributions for vibrationally-exited HNC, HC_3N, and the CH_3OH $9_5 - 10_4E$ (this work) and $13_0 - 12_1A^+$ (Ando et al. 2017) transitions show such spatial similarities, and the CH_3OH molecule possesses numerous inverted (potentially masing) transitions (Müller et al. 2004), we have investigated the possibility that the excitation of these transitions shares a common origin.

To investigate the potential for inverted level populations in the CH_3OH $9_5 - 10_4E$ and $13_0 - 12_1A^+$ transitions, we have run LVG models (RADEX[8]; van der Tak et al. 2007) over representative ranges in n(H_2), N(CH_3OH), and T_K:

- n(H_2) = 10^4 to 10^7 cm^{-3}

- N(CH_3OH) = 10^{13} to 10^{16} cm^{-2}

- T_K = 50 to 300 K

- FWHM linewidth = 50 km/s (typical value from our spectral extraction process (Section 4.2))

Over these ranges in volume density, CH_3OH column density, and kinetic temperature we could not find *any* set of physical conditions where the populations of the CH_3OH $9_5 - 10_4E$ and $13_0 - 12_1A^+$ transitions were *not* inverted. Excitation temperatures for these two transitions range from $T_{ex}(CH_3OH\text{-}A)$ = −8 to −32 K and $T_{ex}(CH_3OH\text{-}E)$ = −21 to −200 K within our LVG models. It appears that amplification of a background continuum source through these two CH_3OH transitions is a plausible explanation for the anomalous spatial distributions measured.

Region 6 contains a rather strong (S(2 cm) = 5.59 mJy; Ulvestad & Antonucci 1997) radio continuum source. As the vibrational transitions from HNC and HC_3N are excited by mid-infrared emission at 21 μm (HNC $4-3$ $\nu_2 = 1f$; Aalto et al. 2007) and 34 μm for (HC_3N $24 - 23$ $\nu_7 = 2$; Wyrowski et al. 1999), we have investigated the potential sources of mid-infrared emission from Region 6. Günthardt et al.

---

[8] http://var.sron.nl/radex/radex.php
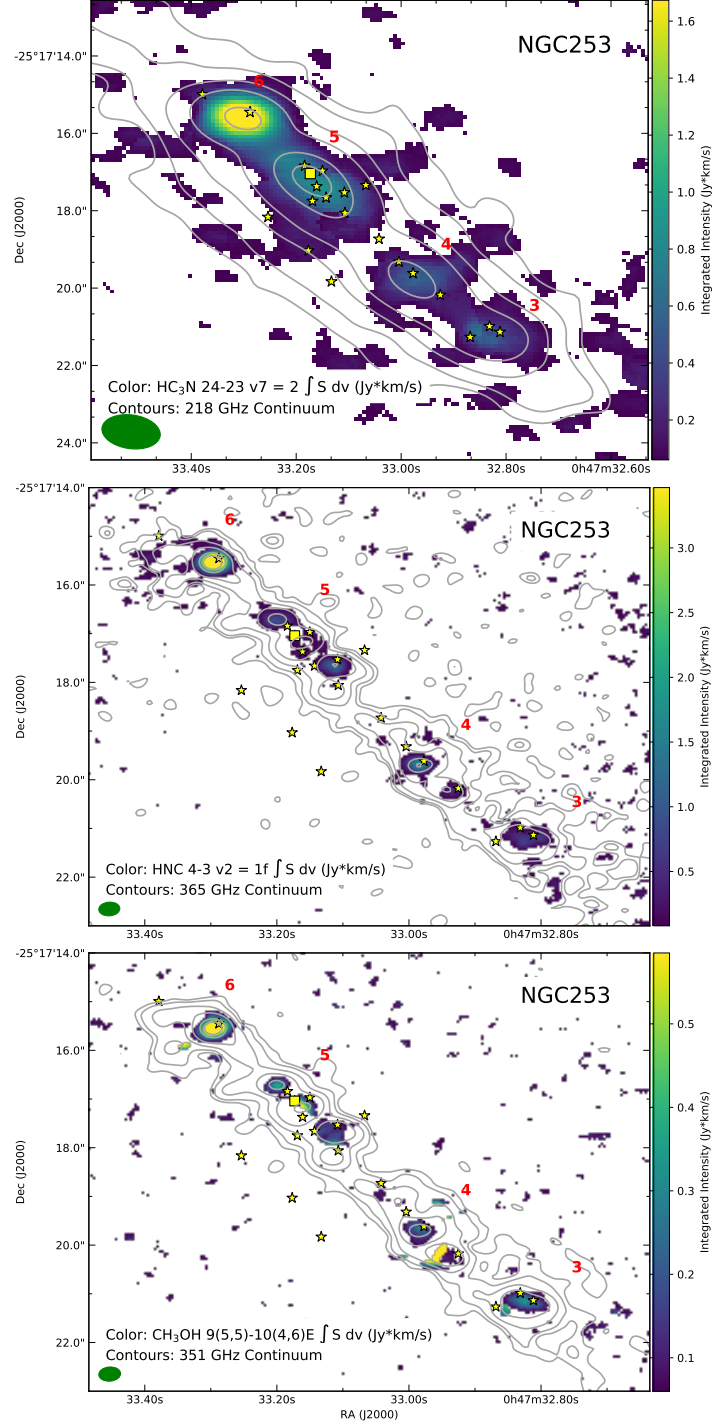
Figure 8. Integrated intensity images for the vibrationally-excited HC$_3$N $24-23$ $\nu_7 = 2$ and HNC $4-3$ $\nu_2 = 1f$ transitions and the CH$_3$OH $9_5 - 10_4 E$ transition. The synthesized beam is displayed in the lower-left of each panel. Red numbers indicate the locations of the dense molecular transition regions identified by Leroy et al. (2015, Table 4). Yellow markers locate the positions of the 2 cm radio continuum emission peaks (Ulvestad & Antonucci 1997), with a square indicating the position of the strongest radio continuum peak identified by Turner & Ho (1985) (TH2: RA(J2000) = 00^h 47^m $33^s.18$, Dec(J2000) = $-25°$ $17'$ $16''.93$). Contour levels are 3, 5, 10, 20, 50, and 75 mJy/beam (218 GHz continuum); 5, 10, 20, 50, and 75 mJy/beam (365 GHz continuum); and 3, 5, 10, 20, 50, and 75 mJy/beam (351 GHz continuum).

(2015) imaged the mid-infrared emission from NGC 253, finding numerous compact sources along the circumnuclear disk. Region 6 corresponds to source A3 in Table 2 of Günthardt et al. (2015), which has a flux of 45 mJy in the infrared Qa-band ($\lambda = 18.3\,\mu m$). In the infrared Q-band ($\lambda = 18.7\,\mu m$) images of Fernández-Ontiveros et al. (2009), a strong unnamed infrared source exists that is within (ΔRA,ΔDec) = (1.0,0.2) arcsec of Region 6. Finally, note that the Qa-band sources A2 and A4 in Günthardt et al. (2015), the brightest mid-infrared sources in NGC 253 with about 1.2 Jy of Qa-band flux (called the "Infrared Core", or "IRC" in many references which describe the infrared properties of NGC 253), are about (ΔRA,ΔDec) = (-4,-3) arcsec away from Region 6, located near Regions 3 and 4.

As there is a strong source of mid-infrared emission associated with the submillimeter continuum and molecular spectral line peaks of Region 6, it seems plausible to suggest that the source(s) of these radio, millimeter, submillimeter, and infrared continuum components may provide the sources of amplification for the vibrationally-excited HC$_3$N $24 - 23\,\nu_7 = 2$ and HNC $4 - 3\,\nu_2 = 1f$ and rotational level inverted CH$_3$OH $9_5 - 10_4 E$ and $13_0 - 12_1 A^+$ transitions. This suggests caution is in order when using these CH$_3$OH transitions to investigate molecular abundance variations within the NGC 253 CMZ.

9. CONCLUSIONS

Combined ALMA 12m Array and ACA imaging at ALMA frequency Band 6 (217.3 to 220.8 GHz) and Band 7 (350.8 to 352.7 GHz; 362.5 to 364.4 and 363.9 to 365.8 GHz) of the CMZ within NGC 253 have been used to characterize the dense gas kinetic temperature structure and its relationship to potential sources of heating in the GMCs within the NGC 253 nucleus. These measurements have yielded the following conclusions:

- Continuum images extracted from our spectral imaging have been used to identify five continuum/gas structures, two with identifiable substructure, within the NGC 253 CMZ. The components identified within our measurements correspond to those identified previously (Sakamoto et al. 2011; Leroy et al. 2015; Meier et al. 2015; Ando et al. 2017; Turner & Ho 1985), and appear to be analogs to giant molecular clouds (GMCs) in our Galaxy.

- Our dust continuum measurements have been used to calculate H$_2$ column densities and masses for all measured GMCs. N(H$_2$) and M(H$_2$) range from $1.29 - 68.09 \times 10^{23}\,\mathrm{cm}^{-2}$ and $0.19 - 23.63 \times 10^6\,\mathrm{M}_\odot$, respectively.

- Using the selected continuum component positions, we have identified fifteen molecular species/isotopologues represented by a total of twenty-nine molecular transitions. Integrated intensities have been extracted from our spectral imaging, which were subsequently used to derive molecular column densities and abundances within the GMCs which comprise the NGC 253 CMZ.

- Using ten transitions from the H_2CO molecule, we derive the kinetic temperature within the $\sim 0.''5$ to $5''$ GMCs. On $\sim 5''$ ($\sim 80\,pc$) scales we measure $T_K \gtrsim 50\,K$, while on size scales $\lesssim 1''$ ($\lesssim 16\,pc$) we measure $T_K \gtrsim 300\,K$, which surpasses the limits of our H_2CO kinetic temperature measurement technique. These kinetic temperature measurements are consistent with those derived from previous lower spatial resolution studies (Mangum et al. 2008, 2013a,b; Gorski et al. 2017).

- Further evidence for the influence of different heating mechanisms within the GMCs of NGC 253 have been identified by comparing the relative abundances of thirteen molecular species within these GMCs to those derived from modified PDR model predictions (Meijerink et al. 2011; Bayet et al. 2011). A general gradient with increasing abundances of cosmic ray and mechanical heating sensitive molecules from the nucleus of NGC 253 to GMCs further out in the nuclear disk is observed. These variations in the molecular abundances among the GMCs in NGC 253 support a cosmic ray heating dominated scenario, but also do not rule out a significant influence due to mechanical heating.

- The simultaneous use of a number of molecular species, as opposed to a single chemical diagnostic, has proven to be an effective indicator of heating processes within the NGC 253 CMZ. These chemical indicators point to cosmic ray and/or mechanical heating as plausible mechanisms by which the GMCs in the CMZ of NGC 253 are heated to the high kinetic temperatures that we measure.

- While investigating the spatial variations among our derived GMC molecular column densities, we noted that vibrationally-excited transitions from HNC and HC_3N are strongly peaked toward an off-nuclear (Region 6) GMC with an associated strong mid-infrared source.

- The Region 6 GMC is also the source of the strongest CH_3OH emission within the NGC 253 CMZ. As numerous CH_3OH transitions are known to have inverted energy level populations, which present as maser emission (i.e. $36.2\,GHz$ $4_{-1} - 3_0 E$), we investigated the potential for our measurements of the CH_3OH $9_5 - 10_4 E$ and the Ando et al. (2017) measurements of the CH_3OH $13_0 - 12_1 A^+$ transition to possess inverted level populations for physical conditions which are representative of the NGC 253 CMZ. LVG models over representative ranges of $n(H_2)$, $N(CH_3OH)$, and T_K indicate that *all* investigated physical conditions produced inverted CH_3OH level populations. Amplification of a background continuum source through these two CH_3OH transitions is a plausible explanation for the anomalous spatial distributions measured.

- A review of the radio through infrared measurements of the center of the NGC 253 nucleus suggests that there is insufficient evidence to support the

existence of a low-luminosity AGN at the center of NGC 253. The radio wavelength emission from NGC 253 is dominated by that from HII regions, radio supernovae, and supernova remnants.

- A search for the sources of the high kinetic temperatures in the NGC 253 GMCs encompassed a study of existing high spatial resolution radio through infrared imaging. Potential sources of cosmic rays and mechanical heating were determined by noting the radio spectral indices from sources in each NGC 253 GMC (Ulvestad & Antonucci 1997). Radio sources with spectral indices in the range $\alpha < -0.4$ are more numerous in the central GMC (Region 5, which contains the Turner & Ho (1985) sources TH2 through TH6) than elsewhere in the NGC 253 CMZ. Radio spectral indices in this range are indicative of synchrotron emission, which can be generated by supernova remnants, which produce cosmic rays and inject mechanical energy into dense gas.

Facility: ALMA

Software: CASA, spectral-cube (Robitaille et al. 2016), PySpecKit (Ginsburg & Mirocha 2011), Astropy (The Astropy Collaboration et al. 2018)

APPENDIX

A. DATA CALIBRATION DETAILS

Table 11 lists the measured and assumed fluxes and uncertainties associated with all of the calibration measurements acquired with our NGC 253 Band 6 and 7 ALMA data. This information is meant to support our estimates of the flux uncertainties associated with the measurements presented.

Table 11. Gain, Flux, and Bandpass Calibrator Fluxes

Measurement	Calibrator	Derived/Assumed Flux [a] (GA,BP:mJy; FL,PT:Jy)	Flux Uncertainty (%)
NGC 253			
Band 6 12m Array Measurement on 2014-12-28			
GA	J0038−2459	341.1±1.8, 339.6±1.9, 330.4±2.1	0.5, 0.6, 0.6
BP	J2258−2758	453.4±1.7, 449.5±1.7, 424.2±2.0	0.4, 0.4, 0.5
FL	Uranus	30.9, 31.3, 34.8	5[b]
PT	J0108+0135	900±130	14
Band 6 12m Array Measurement on 2015-05-02			
GA	J0038−2459	263.8±3.9, 262.4±3.9, 252.5±4.3	1.5, 1.5, 1.7
BP	J0334−4008	688.2±4.8, 685.8±5.5, 653.3±6.5	0.7 0.8, 1.0
FL	Mars	78.5, 79.7, 89.5	10[b]
PT	J0238+1636	1550±50	3
Band 6 ACA Measurement on 2014-06-04			
GA	J0038−2459	458.4±4.6, 453.5±4.6, 422.4±5.2	1.0, 1.0, 1.2
BP	J2258−2758	570.7±2.3, 569.3±2.6, 521.5±3.4	0.4, 0.4, 0.6
FL	Neptune	13.0, 13.1, 13.6	10[b]
Band 6 ACA Measurement on 2014-06-04			
GA	J0038−2459	450.6±4.0, 448.0±5.8, 425.1±4.8	0.9, 1.3, 1.1
BP	J2258−2758	570.7±2.4, 567.7±2.7, 538.6±3.0	0.4, 0.5, 0.5
FL	Uranus	28.9, 29.3, 32.6	5[b]
Band 6 ACA Measurement on 2014-06-04			
GA	J0038−2459	445.5±4.6, 442.4±5.3, 427.7±4.0	1.0, 1.0, 1.2
BP	J2258−2758	559.4±2.7, 554.2±2.6, 528.3±2.4	0.4, 0.4, 0.6
FL	Uranus	28.9, 29.3, 32.6	5[b]
Band 7 12m Array Measurement on 2014-05-19			
GA	J0038−2459	290.0±12.5, 287.5±16.6, 289.2±18.5	4.3, 5.8, 6.4
BP	J0006−0623	2092.47±34.6, 2074.5±45.7, 2066.6±48.4	1.7, 2.2, 2.3
FL	J2258−2758	0.4±0.1[c]	15[c]
Band 7 ACA Measurement on 2014-05-19			
GA	J0038−2459	274.7±8.2, 279.9±7.5, 284.1±11.2	3.0, 2.7, 3.9
BP	J0006−0623	2045.2±14.0, 2080.7±10.6, 2066.0±10.8	0.7, 0.5, 0.5
FL	Neptune	25.8, 27.7, 27.8	10[b]
Band 7 ACA Measurement on 2014-06-08			
GA	J0038−2459	324.3±7.7, 324.9±9.3, 320.3±6.1	3.0, 2.7, 3.9
BP	J0006−0623	2243.8±15.4, 2214.2±17.5, 2226.3±15.6	0.7, 0.8, 0.7
FL	Uranus	63.8, 66.3, 66.6	5[b]

Table 11 continued on next page

Table 11 *(continued)*

Measurement	Calibrator	Derived/Assumed Flux [a]	Flux Uncertainty (%)
		(GA,BP:mJy; FL,PT:Jy)	

[a]Derived (GA and BP) or assumed (FL and PT) flux, where GA $\equiv$ gain amplitude, BP $\equiv$ bandpass, FL $\equiv$ flux, and PT $\equiv$ pointing calibration.

[b]See discussion in Section 2.

[c]Assumed flux from ALMA calibrator catalog.

B. SPECTRAL PROPERTIES

Table 12 lists the frequency, upper state energy, line strength, dipole moment, and transition degeneracies for each measured transition.

Table 12. Measured Transition Spectral Properties

Molecule	Transition	Frequency (MHz)	E_u (K)	μ (Debye)	S^a	$g_J/g_K/g_I$	$Q_{rot}(50/150/300)$
^{13}CO	$2-1$	220398.684	15.8662	0.11046	$\frac{2}{5}$	5/1/1	19.22/56.97/113.86
C^{18}O	$2-1$	219560.358	15.8059	0.11079	$\frac{2}{5}$	5/1/1	19.31/57.19/114.29
^{13}CN^b	$F_1=3-2$	217467.150	15.684	1.45	$\frac{2}{5}$	5/1/1	19.47/57.74/115.42
SiS	$12-11$	217817.663	67.954	1.730	$\frac{12}{25}$	25/1/1	114.99/344.17/689.59
SO	6_5-5_4	219949.442	34.9847	1.55	$\frac{5}{11}$	13/1/0.5	41.83/137.83/283.33
SO$_2$	$4_{22}-3_{13}$	235151.72	19.0298	1.6331	0.1906	9/1/1	401.17/2084.56/5896.02
SO$_2$	$5_{33}-4_{22}$	351257.224	35.88646	1.6331	0.2495	11/1/1	401.17/2084.56/5896.02
SO$_2$	$14_{4,10}-14_{3,11}$	351873.873	135.87076	1.6331	0.2538	29/1/1	401.17/2084.56/5896.02
HNC	$4-3$	362630.30	43.5097	3.05	$\frac{4}{9}$	9/1/1	23.29/69.18/138.31
OCS	$30-29$	364748.960	271.379	0.7152	$\frac{30}{61}$	61/1/1	171.46/513.44/1028.60
HNCO	10_0-9_0	219798.27	58.0194	1.602	$\frac{10}{21}$	21/1/1	181.60/945.23/2695.60
HNCO	10_1-9_1	218981.02	101.079	1.602	$\frac{99}{210}$	21/1/1	181.60/945.23/2695.60
HNCO	10_2-9_2	219737.19	228.2851	1.602	$\frac{48}{105}$	21/1/1	181.60/945.23/2695.60
H$_2$CO	$3_{03}-2_{02}$	218222.192	20.957	2.332	$\frac{9}{21}$	7/1/0.25	50.14/258.97/731.44
H$_2$CO	$3_{21}-2_{20}$	218760.071	68.112	2.332	$\frac{5}{21}$	7/1/0.25	50.14/258.97/731.44
H$_2$CO	$5_{05}-4_{04}$	362736.048	52.313	2.332	$\frac{25}{55}$	11/1/0.25	50.14/258.97/731.44
H$_2$CO	$5_{24}-4_{23}$	363945.894	99.539	2.332	$\frac{21}{55}$	11/1/0.25	50.14/258.97/731.44
H$_2$CO	$5_{23}-4_{22}$	365363.428	99.658	2.332	$\frac{21}{55}$	11/1/0.25	50.14/258.97/731.44
H$_2$CO	5_4-4_4	364103.249	240.730	2.332	$\frac{9}{55}$	11/1/0.25	50.14/258.97/731.44
H$_2$CO	$5_{15}-4_{14}$	351768.645	64.453	2.332	$\frac{24}{55}$	11/1/0.75	50.14/258.97/731.44
H$_2$CO	5_3-4_3	364288.884	158.424	2.332	$\frac{16}{55}$	11/1/0.75	50.14/258.97/731.44

Table 12 continued on next page

Table 12 (*continued*)

Molecule	Transition	Frequency (MHz)	E_u (K)	μ (Debye)	S^a	$g_J/g_K/g_I$	$Q_{rot}(50/150/300)$
H_3O^+	$3_2 - 2_2$	364797.427	139.338	1.44	$\frac{5}{21}$	7/2/0.25	4.39/22.79/64.46
HC_3N	$24 - 23\ v_0$	218324.72	130.982	3.73172	$\frac{24}{49}$	49/1/1	229.10/686.25/1374.92
HC_3N	$40 - 39$	363785.40	357.9731	3.73172	$\frac{40}{81}$	81/1/1	229.10/686.25/1374.92
C_4H	N=23-22	218857.0	126.05	0.90	23.0	47/1/1	221.05/439.60/1315.80
CH_3CN	$12 - 11, K = 0 - 3$	220747.259	68.8657	3.92197	$\frac{12}{25}$	25/1/0.5	167.17/876.86/2500.55
CH_3OH	$9_{55}-10_{46}E$	351236.343	240.50455	1.412	0.6908	19/1/0.25	72.65/377.50/1067.74

[a]Line strengths calculated using Mangum & Shirley (2015) excluding the following: (SO: Tiemann 1974), (SO_2: Lovas 1985), (CH_3OH: Xu & Lovas 1997).

[b]Strongest component of the hyperfine group with N=2 − 1, J=$\frac{5}{2}$ − $\frac{3}{2}$.

C. SPECTRAL LINE INTEGRATED INTENSITY IMAGES

Figures 9 through 25 show the spectral line integrated intensities derived from our ALMA Band 6 and 7 imaging of NGC 253. As was shown in the other integrated intensity figures in this article, red numbers indicate the locations of the dense molecular transition regions identified by Leroy et al. (2015, Table 4), while yellow markers locate the positions of the 2 cm radio continuum emission peaks (with a square indicating the position of the strongest radio continuum peak) identified by Turner & Ho (1985) (TH2: RA(J2000) = $00^h \, 47^m \, 33^s.18$, Dec(J2000) = $-25° \, 17' \, 16''.93$). Contour levels shown are 3, 5, 10, 20, 50, and 75 mJy/beam (218 GHz continuum); 1, 3, 5, 10, 20, 50, and 75 mJy/beam (219 GHz continuum); 3, 5, 10, 20, 50, and 75 mJy/beam (351 GHz continuum); and 5, 10, 20, 50, and 75 mJy/beam (365 GHz continuum). Note that the spatial distribution is limited by the primary beam of our measurements for our ^{13}CO and C^{18}O $3 - 2$ integrated intensity images (Figure 9). For this reason we consider our measurements of these two integrated intensity distributions to not be a completely accurate representation of the spatial distribution on the ^{13}CO and C^{18}O distributions in NGC 253.

REFERENCES

Aalto, S., Spaans, M., Wiedner, M. C., & Hüttemeister, S. 2007, A&A, 464, 193

Acero, F., Aharonian, F., Akhperjanian, A. G., et al. 2009, Science, 326, 1080

Aladro, R., Martín, S., Riquelme, D., et al. 2015, A&A, 579, A101

Ando, R., Nakanishi, K., Kohno, K., et al. 2017, ApJ, 849, 81

Ao, Y., Henkel, C., Menten, K. M., et al. 2013, A&A, 550, A135

Bayet, E., Williams, D. A., Hartquist, T. W., & Viti, S. 2011, MNRAS, 414, 1583

Brunthaler, A., Castangia, P., Tarchi, A., et al. 2009, A&A, 497, 103

Carroll, T. J., & Goldsmith, P. F. 1981, ApJ, 245, 891

Chen, X., Ellingsen, S. P., Shen, Z.-Q., et al. 2018, ApJL, 856, L35

Condon, J. J. 1992, ARA&A, 30, 575

Costagliola, F., Aalto, S., Sakamoto, K., et al. 2013, A&A, 556, A66

Costagliola, F., Sakamoto, K., Muller, S., et al. 2015, A&A, 582, A91

Cotton, W. D. 2017, Publications of the Astronomical Society of the Pacific, 129, 094501

Draine, B. T. 2011, Physics of the Interstellar and Intergalactic Medium (Physics of the Interstellar and Intergalactic Medium by Bruce T. Draine. Princeton University Press, 2011. ISBN: 978-0-691-12214-4)

Ellingsen, S. P., Chen, X., Breen, S. L., & Qiao, H.-h. 2017, ApJL, 841, L14

Ellingsen, S. P., Chen, X., Qiao, H.-H., et al. 2014, ApJL, 790, L28

Fernández-Ontiveros, J. A., Prieto, M. A., & Acosta-Pulido, J. A. 2009, MNRAS, 392, L16

Ginsburg, A., & Mirocha, J. 2011, PySpecKit: Python Spectroscopic Toolkit, Astrophysics Source Code Library, ascl:1109.001

Ginsburg, A., Henkel, C., Ao, Y., et al. 2016, A&A, 586, A50

Gorski, M., Ott, J., Rand, R., et al. 2017, ApJ, 842, 124

Gorski, M. D., Ott, J., Rand, R., et al. 2018, MNRAS, 2932

Green, S. 1991, ApJS, 76, 979

Günthardt, G. I., Agüero, M. P., Camperi, J. A., et al. 2015, AJ, 150, 139

Hildebrand, R. H. 1983, QJRAS, 24, 267
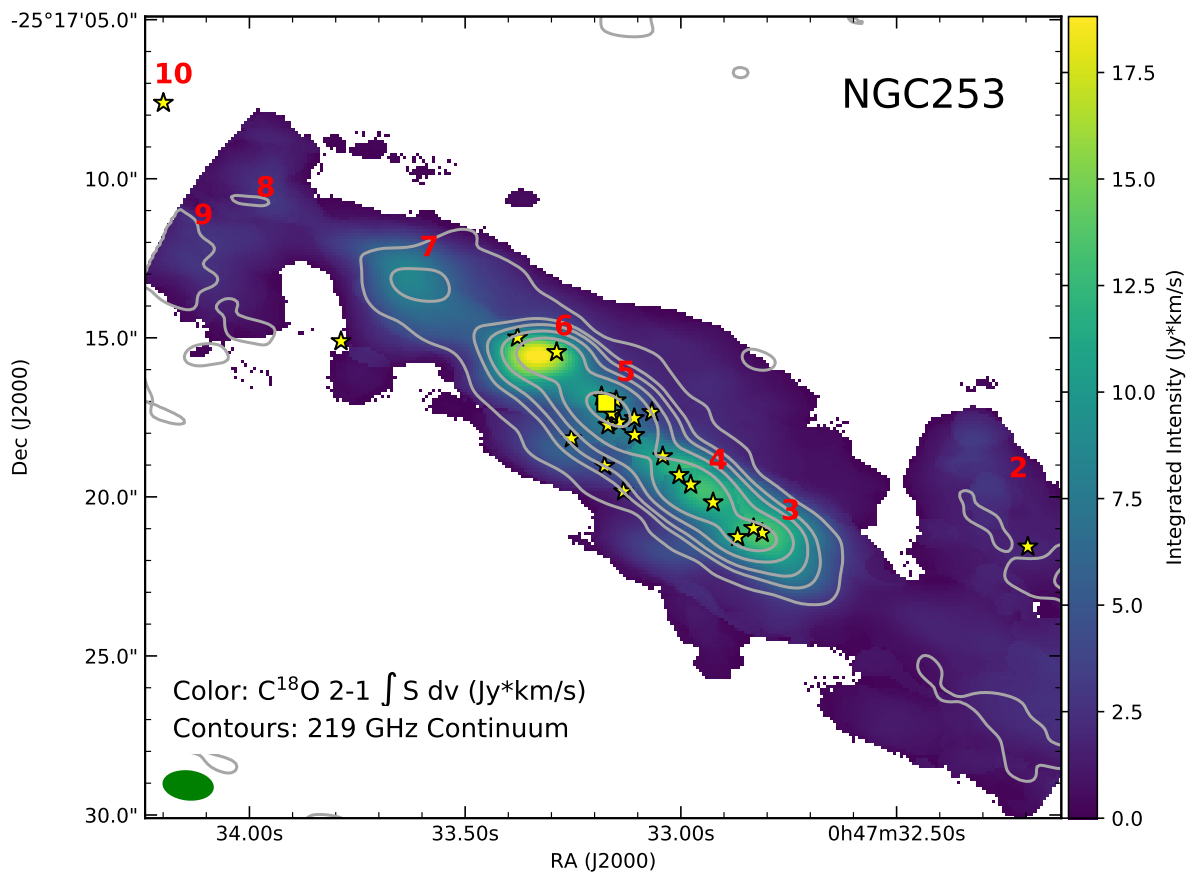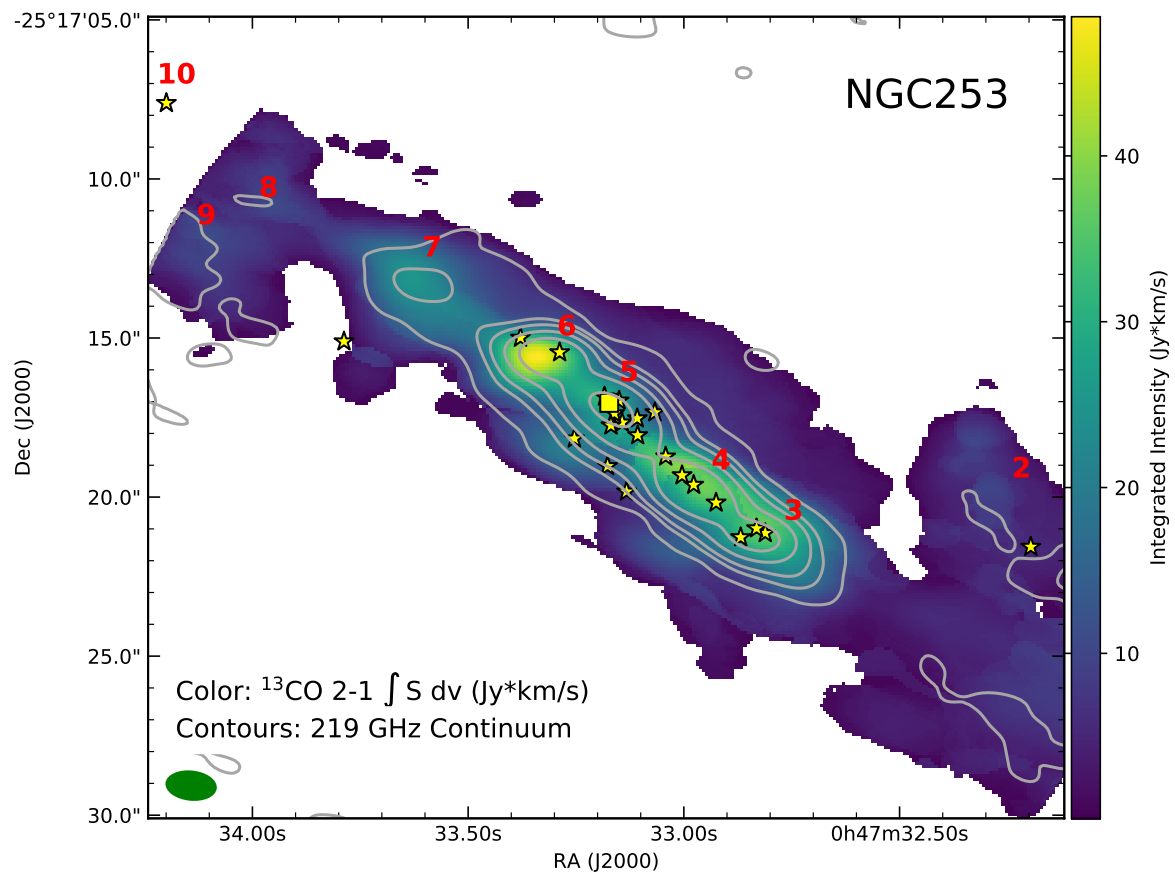
Figure 9. $^{13}CO\ 2-1$ (top) and $C^{18}O\ 2-1$ (bottom) integrated intensity.

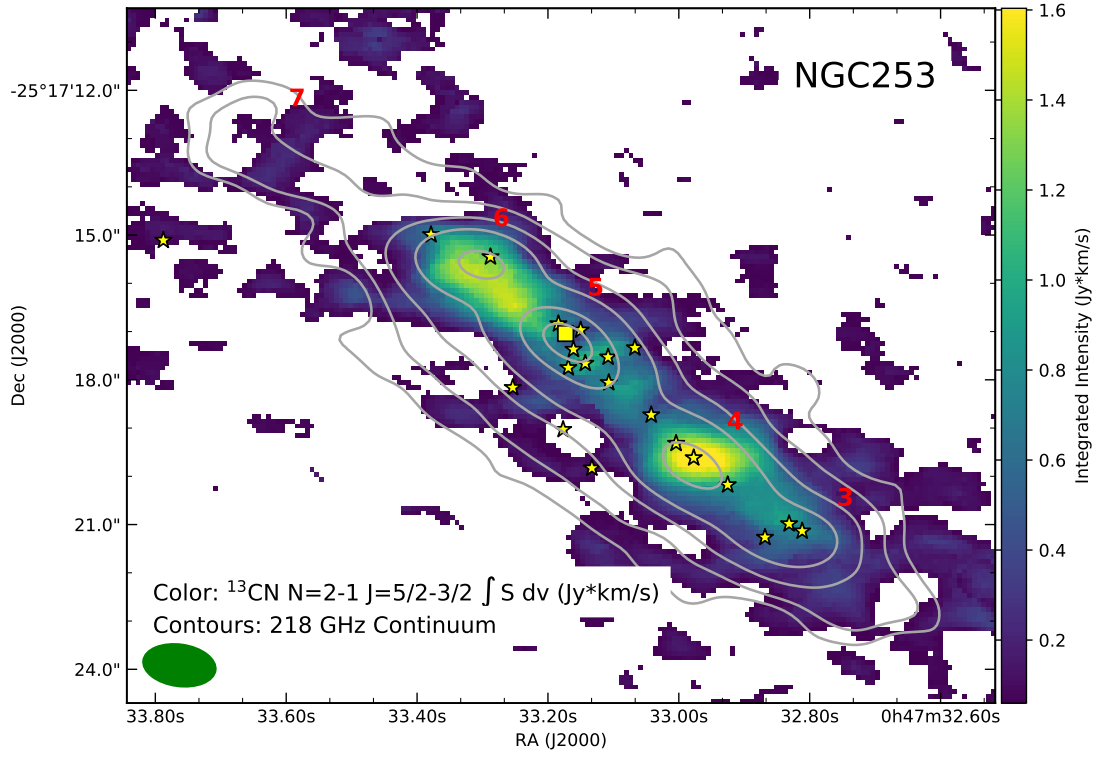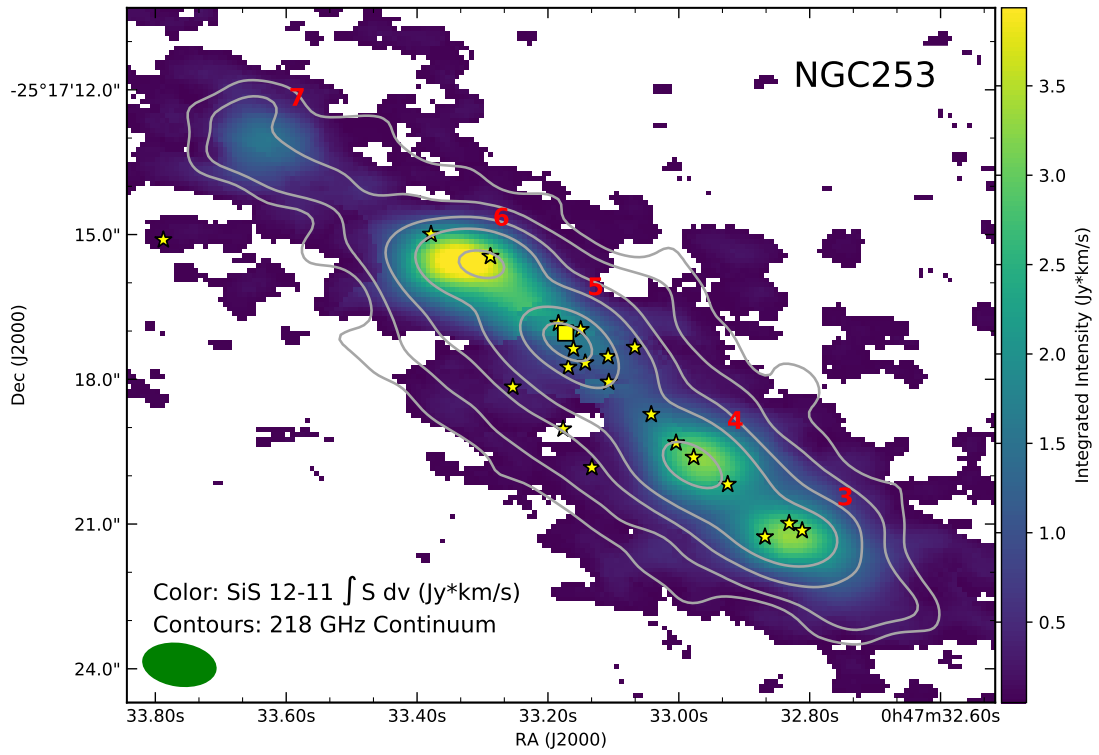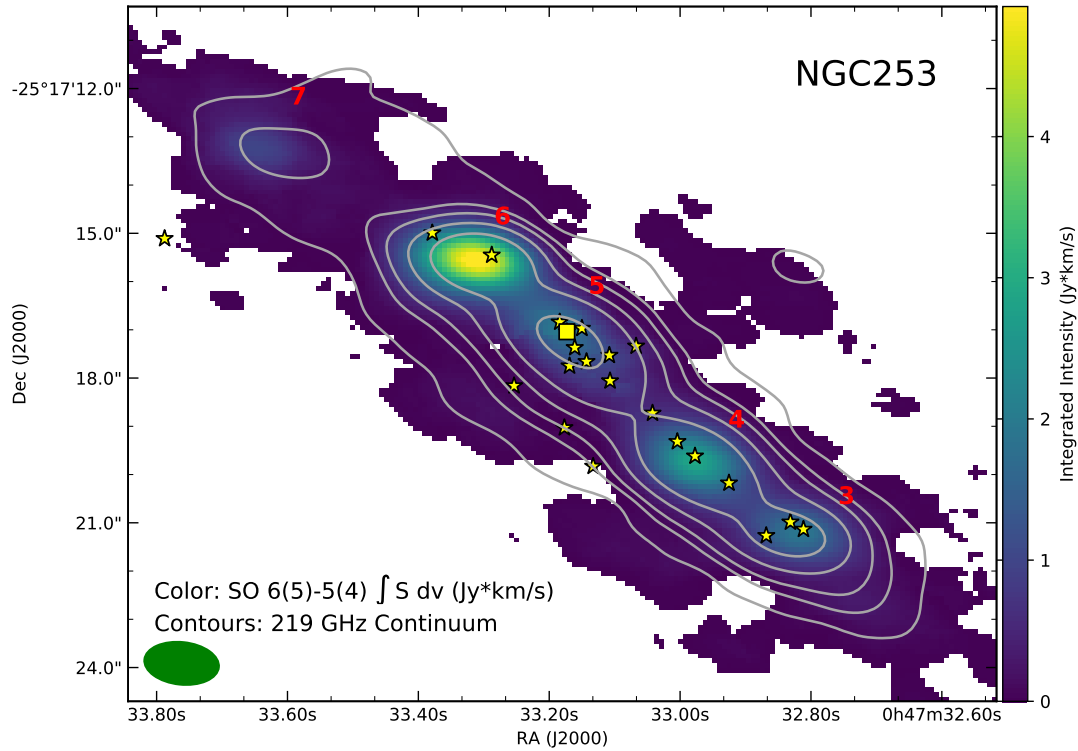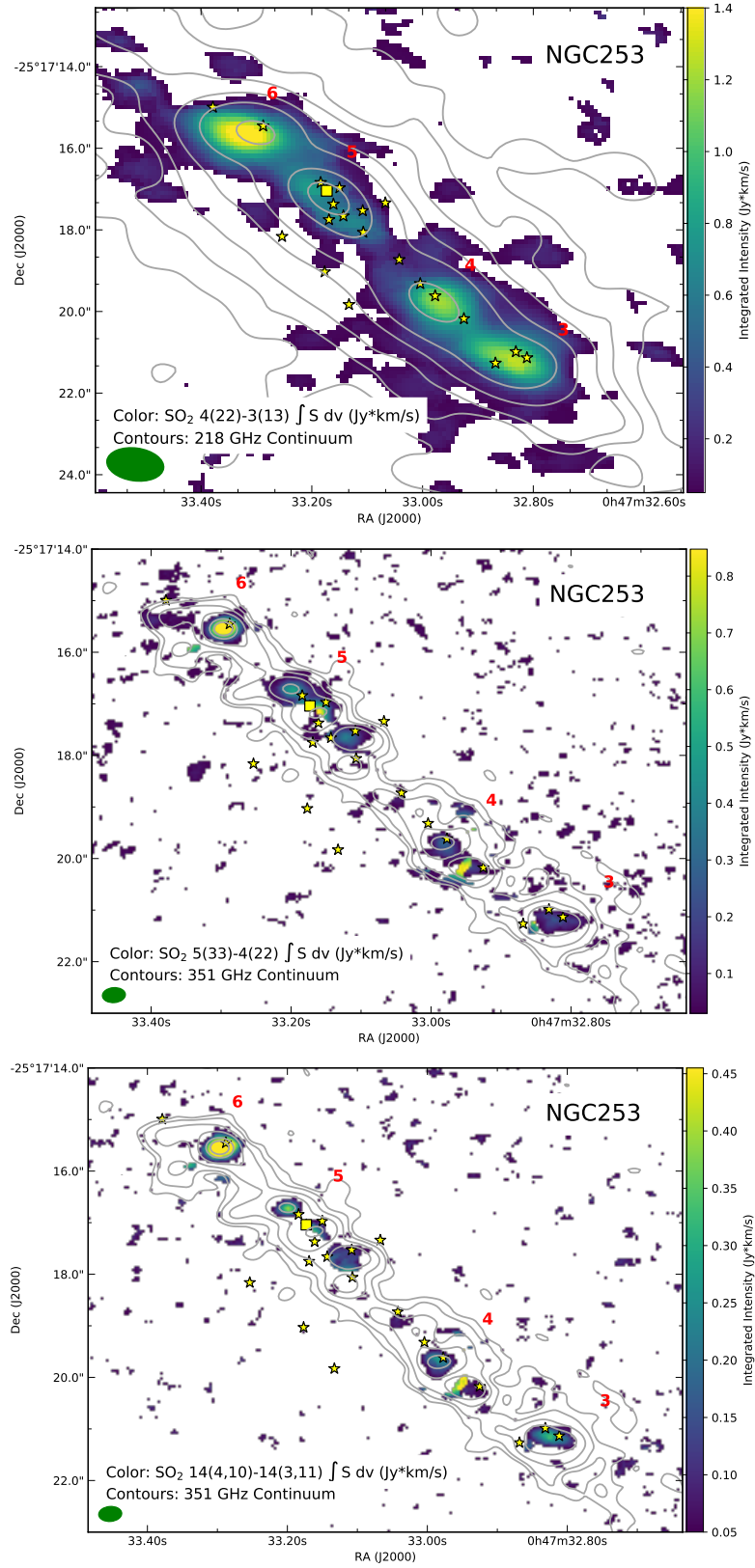**Figure 10.** ^{13}CN $F_1 = 3 - 2$ integrated intensity.
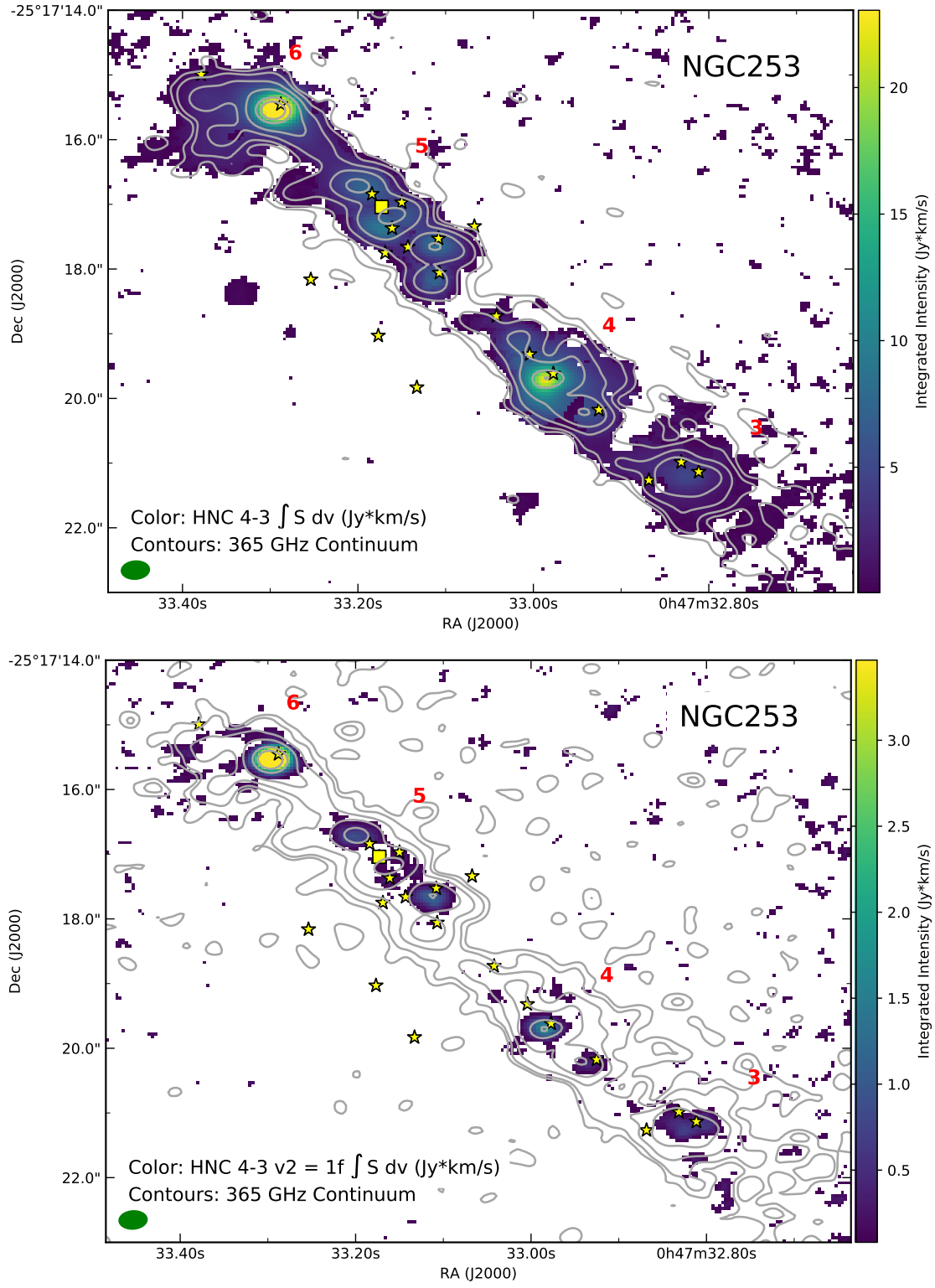

Figure 11. SiS $12 - 11$ integrated intensity.
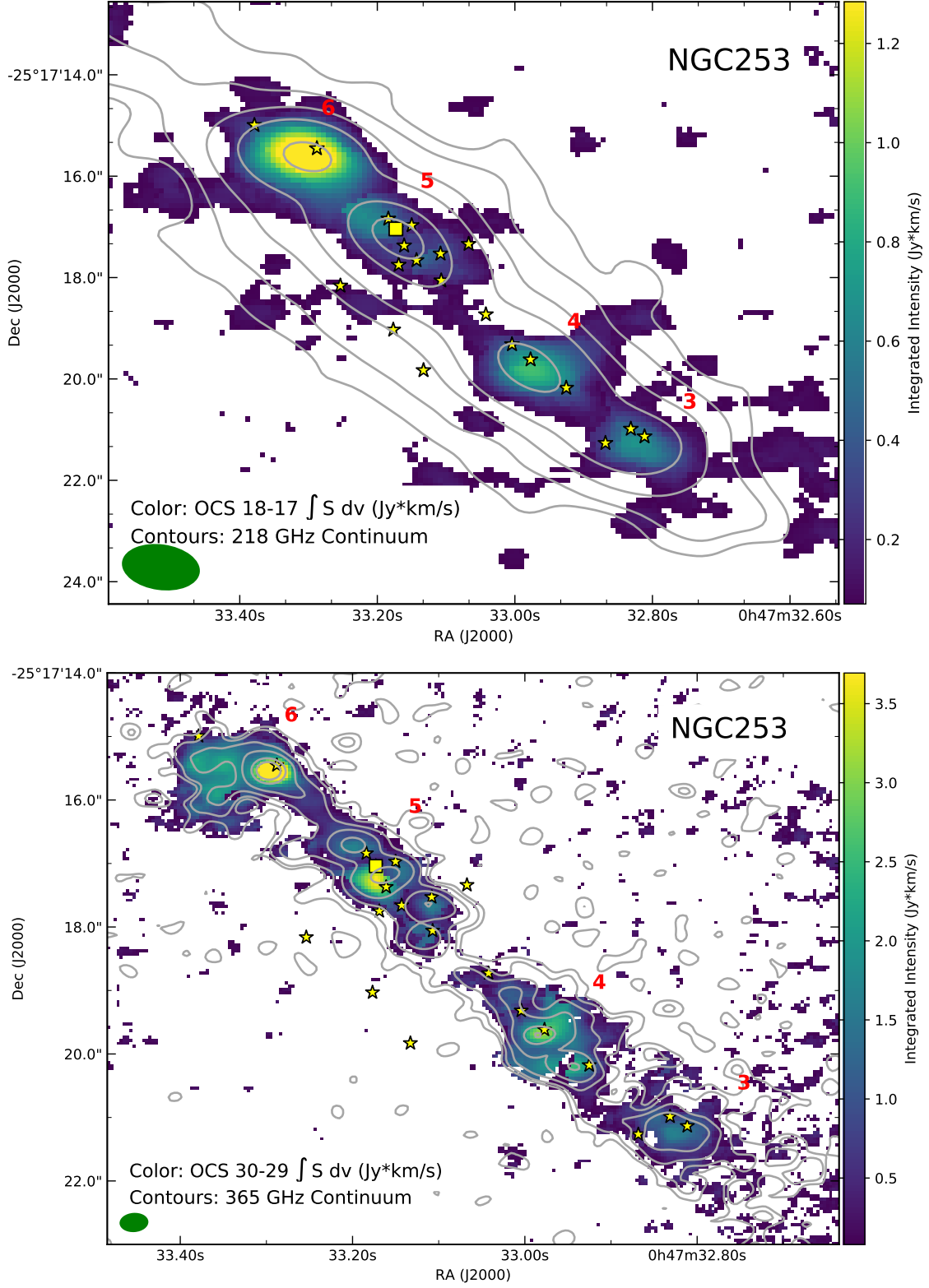
Figure 12. SO $6_5 - 5_4$ integrated intensity.

Imanishi, M., Nakanishi, K., & Izumi, T. 2016, ApJ, 825, 44

Jenkins, E. B. 2009, ApJ, 700, 1299

Kalari, V. M., Rubio, M., Elmegreen, B. G., et al. 2018, ApJ, 852, 71

Leroy, A. K., Bolatto, A. D., Ostriker, E. C., et al. 2015, ApJ, 801, 25

—. 2018, ArXiv e-prints, arXiv:1804.02083

Lovas, F. J. 1985, Journal of Physical and Chemical Reference Data, 14, 395

—. 1992, Journal of Physical and Chemical Reference Data, 21, 181

Mangum, J. G., Darling, J., Henkel, C., & Menten, K. M. 2013a, ApJ, 766, 108

Mangum, J. G., Darling, J., Henkel, C., et al. 2013b, ApJ, 779, 33

Mangum, J. G., Darling, J., Menten, K. M., & Henkel, C. 2008, ApJ, 673, 832

Mangum, J. G., & Shirley, Y. L. 2015, PASP, 127, 266

Mangum, J. G., & Wootten, A. 1993, ApJS, 89, 123

Martín, S., Mauersberger, R., Martín-Pintado, J., Henkel, C., & García-Burillo, S. 2006, ApJS, 164, 450

Mason, B. S., & Brogan, C. 2013, Relative Integration Times for the ALMA Cycle 1 12-m, 7-m, and Total Power Arrays, Tech. Rep. 598, National Radio Astronomy Observatory, Charlottesville, VA 22903, USA

McCormick, A., Veilleux, S., & Rupke, D. S. N. 2013, ApJ, 774, doi:10.1088/0004-637X/774/2/126

Meier, D. S., & Turner, J. L. 2012, ApJ, 755, 104

Meier, D. S., Walter, F., Bolatto, A. D., et al. 2015, ApJ, 801, 63

Meijerink, R., Spaans, M., Loenen, A. F., & van der Werf, P. P. 2011, A&A, 525, A119

Mills, E. A. C., & Morris, M. R. 2013, ApJ, 772, 105

Müller, H. S. P., Menten, K. M., & Mäder, H. 2004, A&A, 428, 1019

Müller, H. S. P., Thorwirth, S., Roth, D. A., & Winnewisser, G. 2001, A&A, 370, L49

Figure 13. SO$_2$ $4_{22} - 3_{13}$ (top), $5_{33} - 4_{22}$ (middle), and $14_{4,10} - 14_{3,11}$ (bottom) integrated intensity.
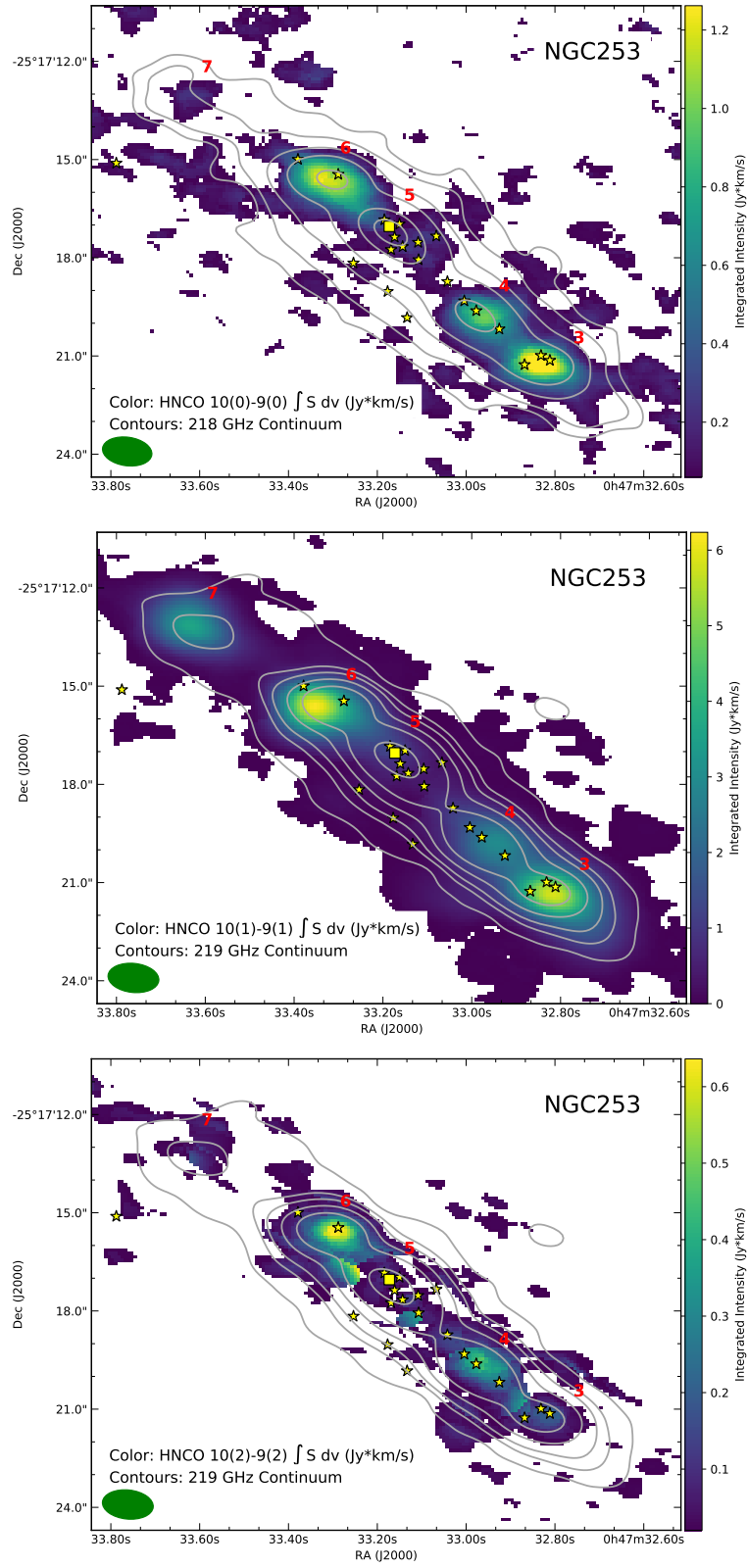
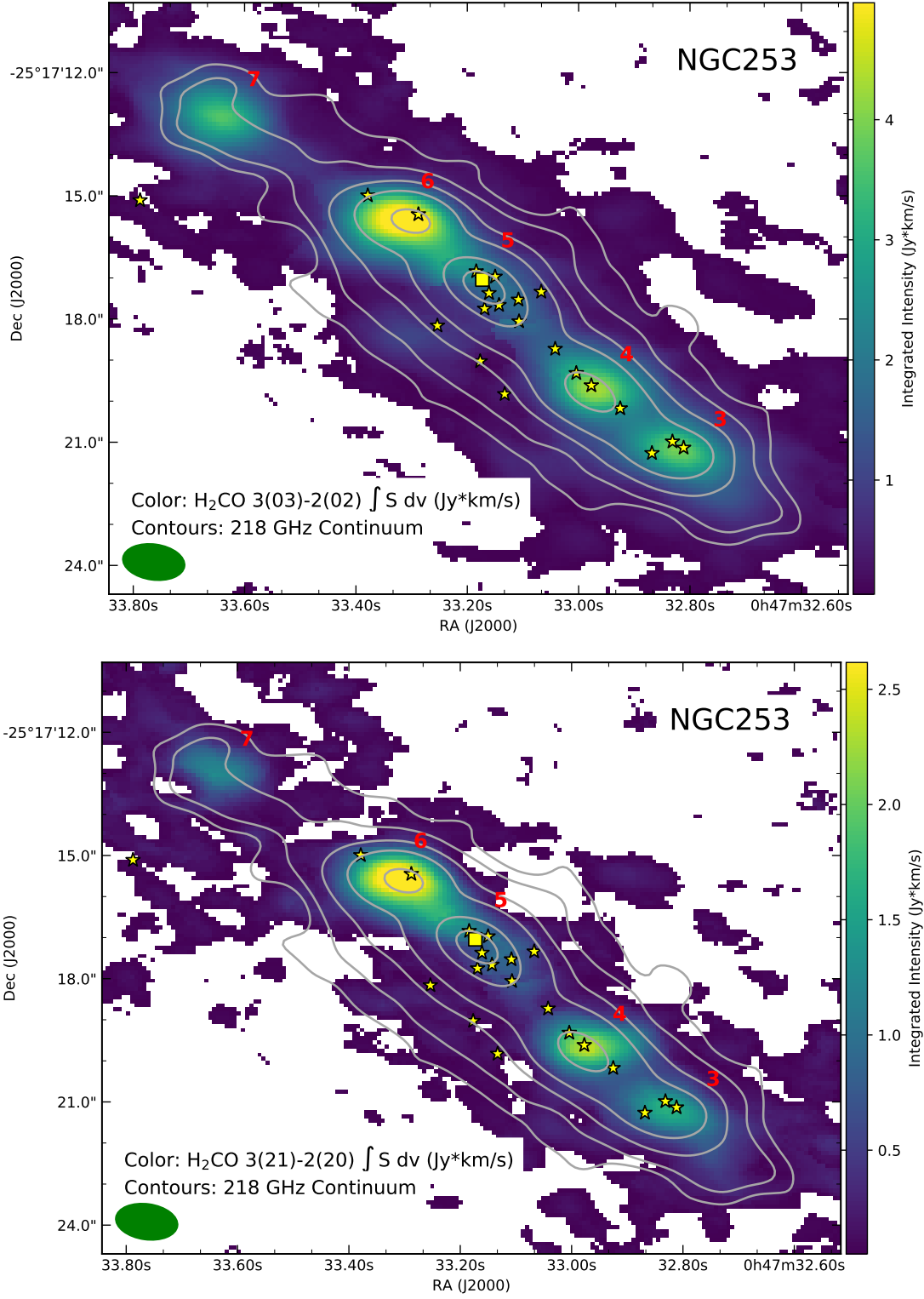**Figure 14.** HNC $4-3$ (top) and $4-3$ $v_2 = 1f$ (bottom) integrated intensity.

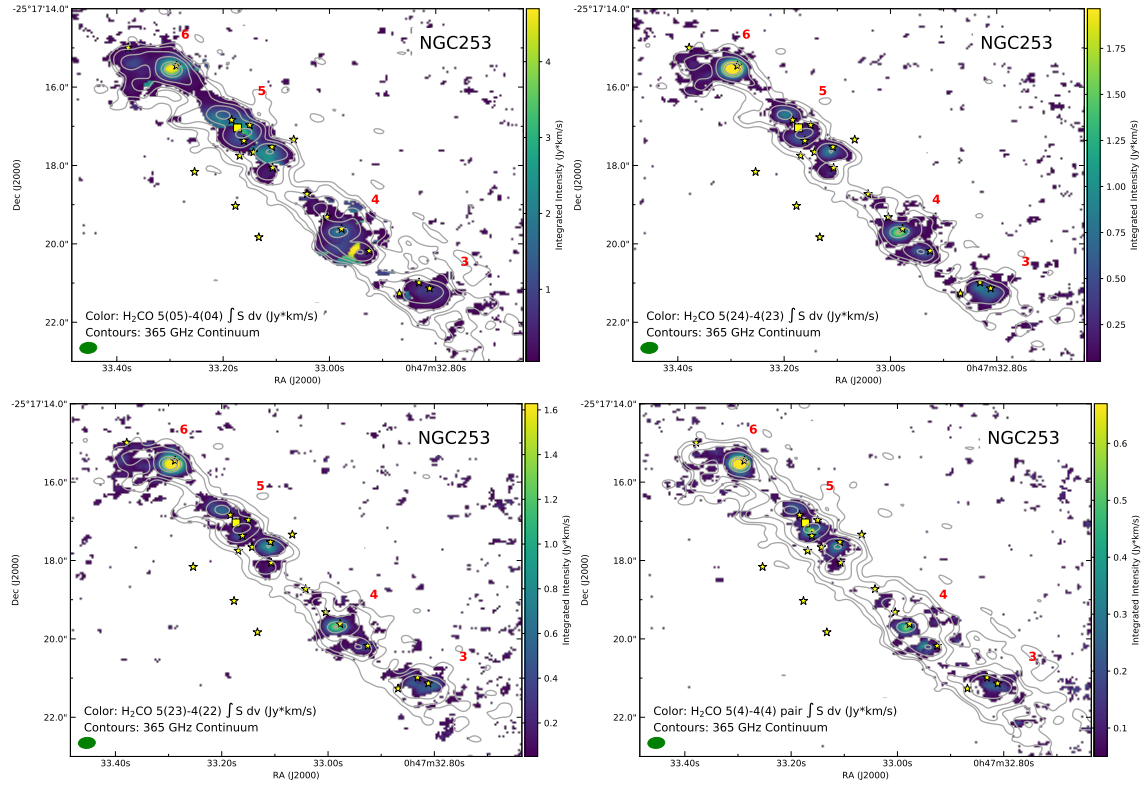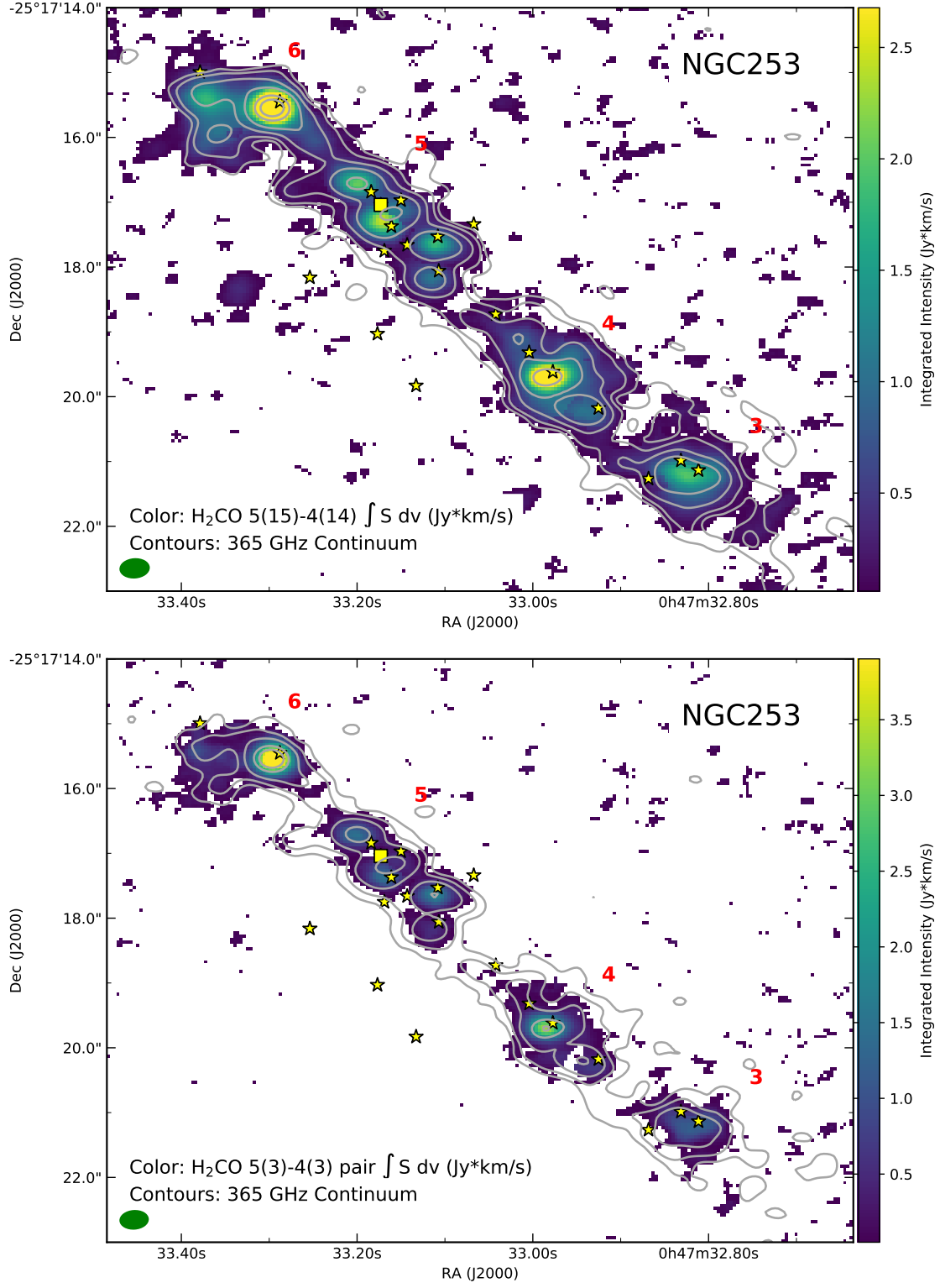**Figure 15.** OCS $18 - 17$ (top) and $30 - 29$ (bottom) integrated intensity.

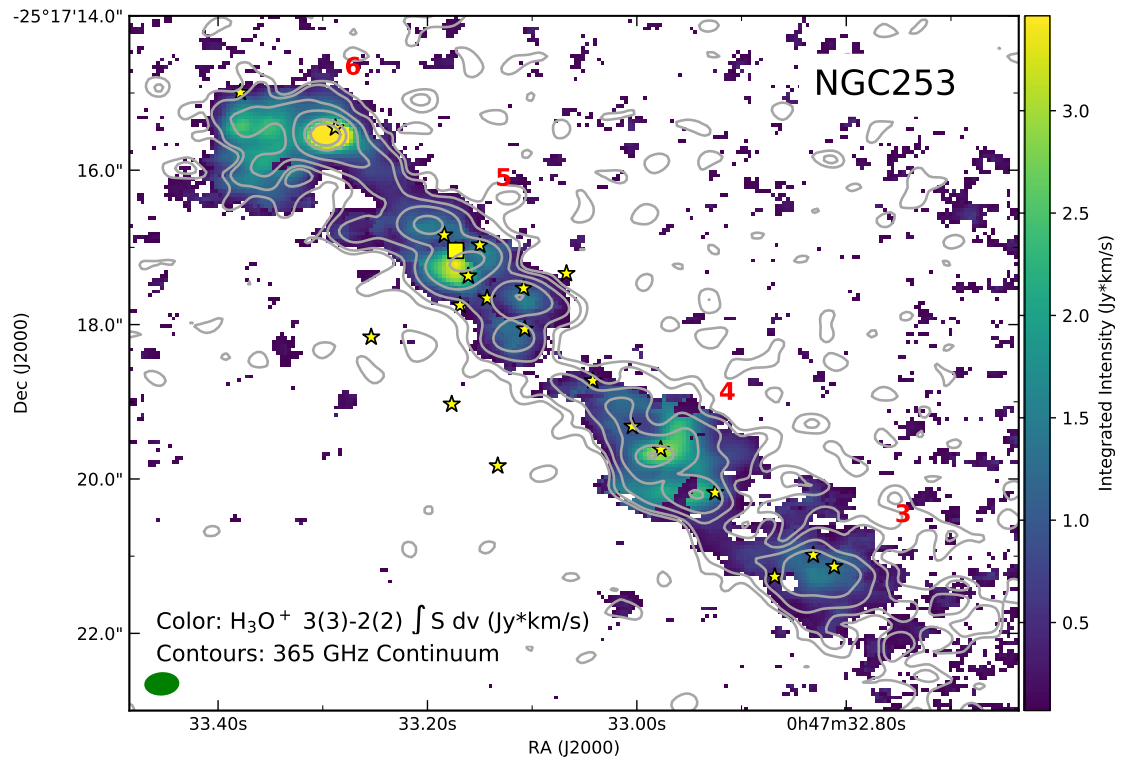**Figure 16.** HNCO 10_0-9_0 (top), 10_1-9_1 (middle), 10_2-9_2 (bottom) integrated intensity.

Figure 17. Para H_2CO $3_{03} - 2_{02}$ (top) and $3_{21} - 2_{20}$ (bottom) integrated intensity.

Figure 18. Para H$_2$CO $5_{05} - 4_{04}$ (top left), $5_{24} - 4_{23}$ (top right), $5_{23} - 4_{22}$ (bottom left), and $5_4 - 4_4$ (bottom right) integrated intensity.

Figure 19. Ortho H$_2$CO $5_{15} - 4_{14}$ (top) and $5_3 - 4_3$ (bottom) integrated intensity.

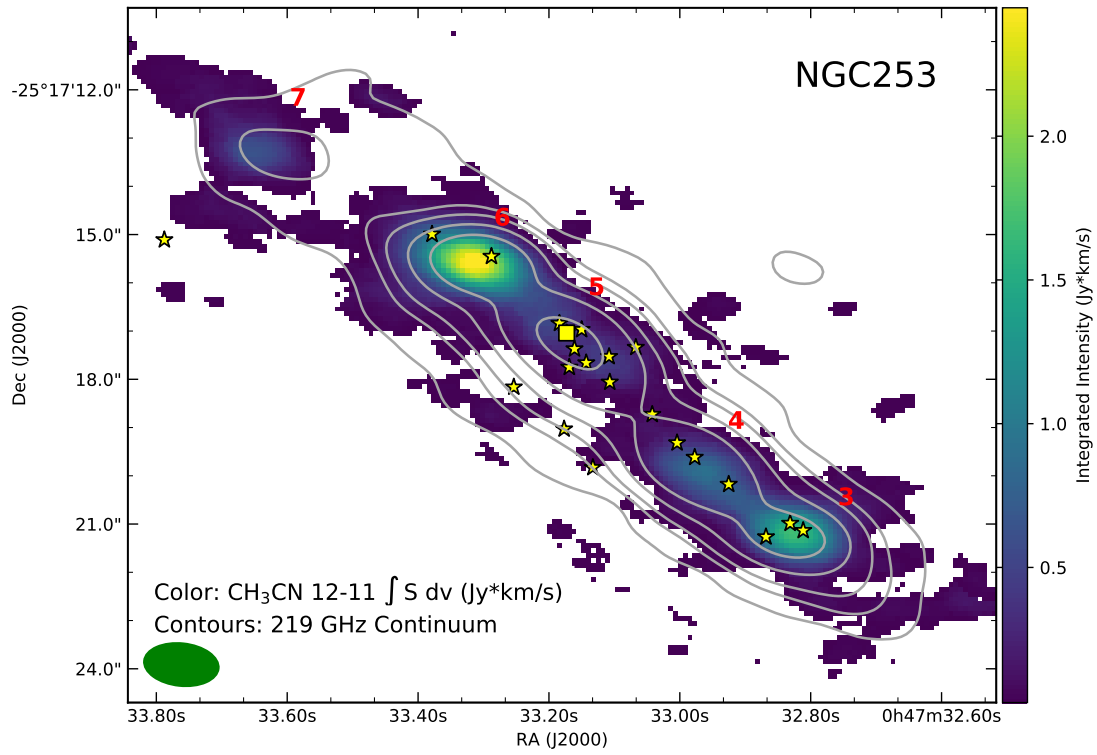**Figure 20.** H_3O^+ $3_2 - 2_2$ integrated intensity.
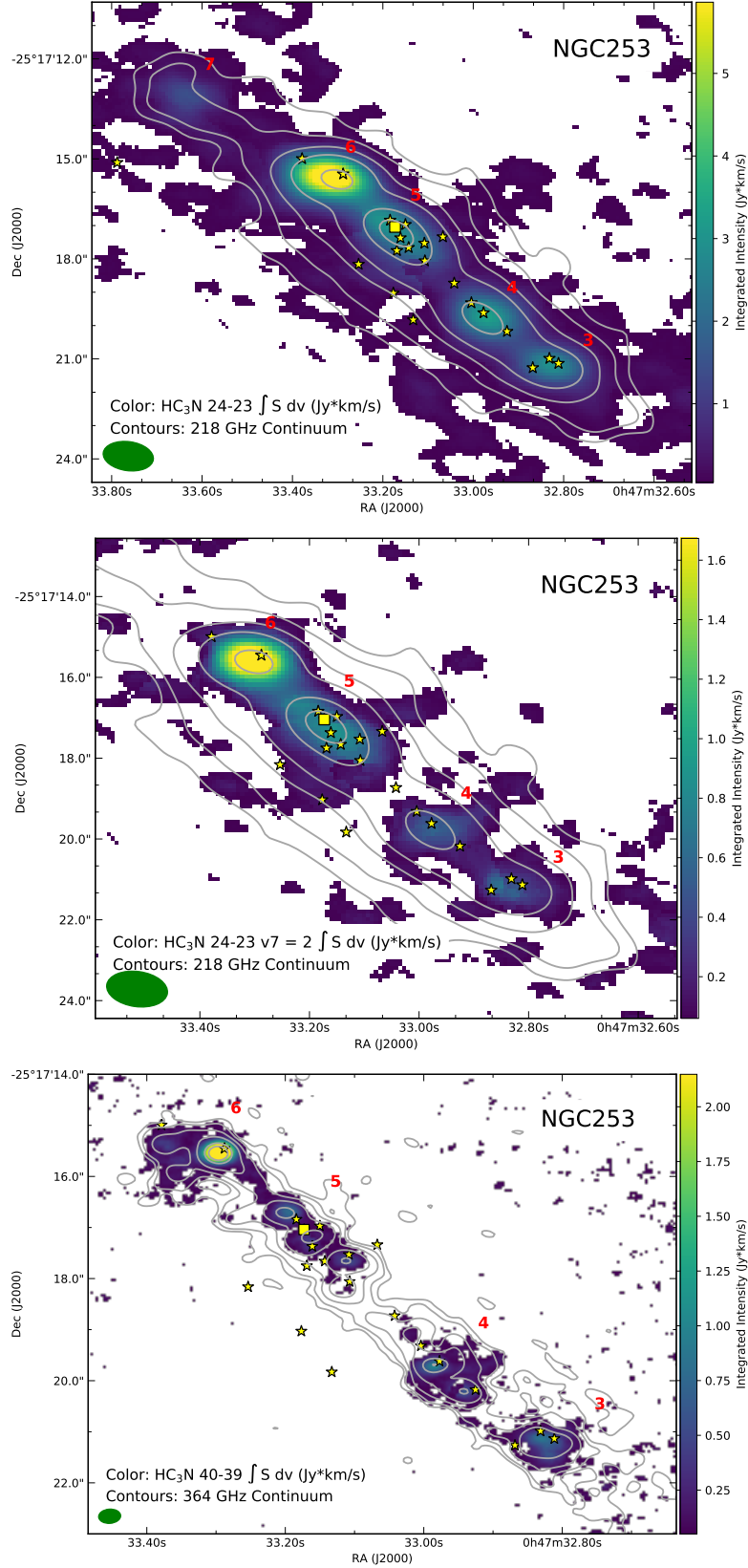
Figure 21. HC$_3$N $24 - 23$ (top), $24 - 23\nu_7 = 2$ (middle), and $40 - 39$ (bottom) integrated intensity.
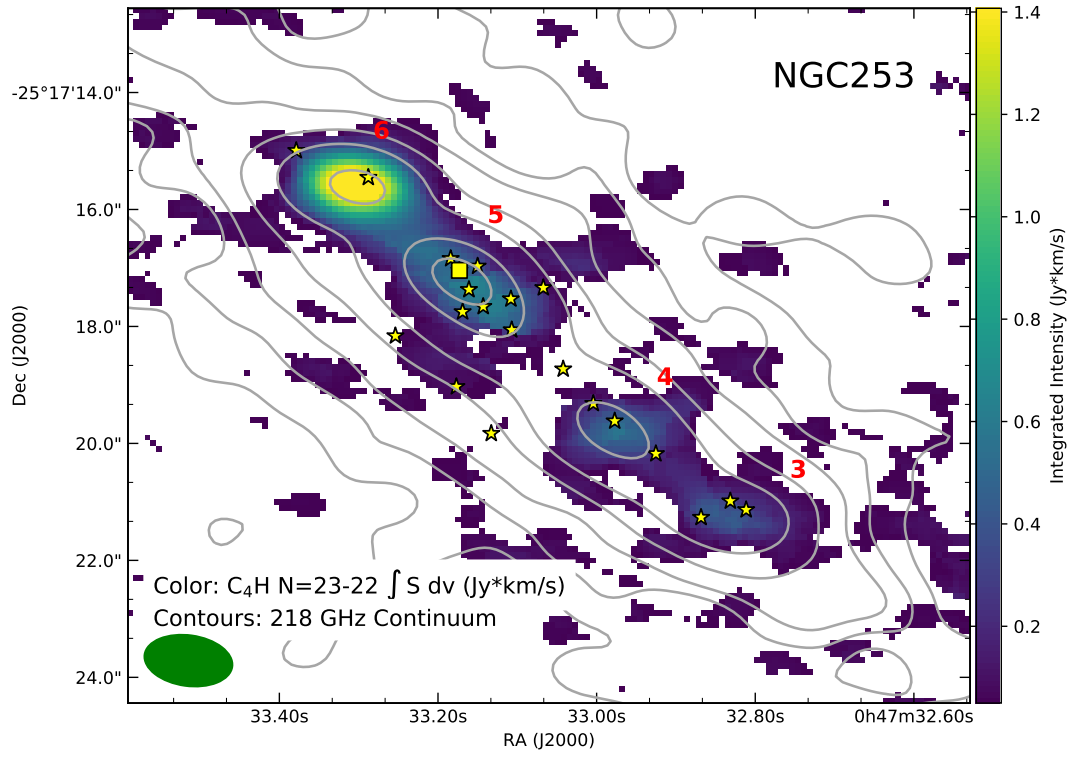
Figure 22. C_4H N$=23-22$ integrated intensity.

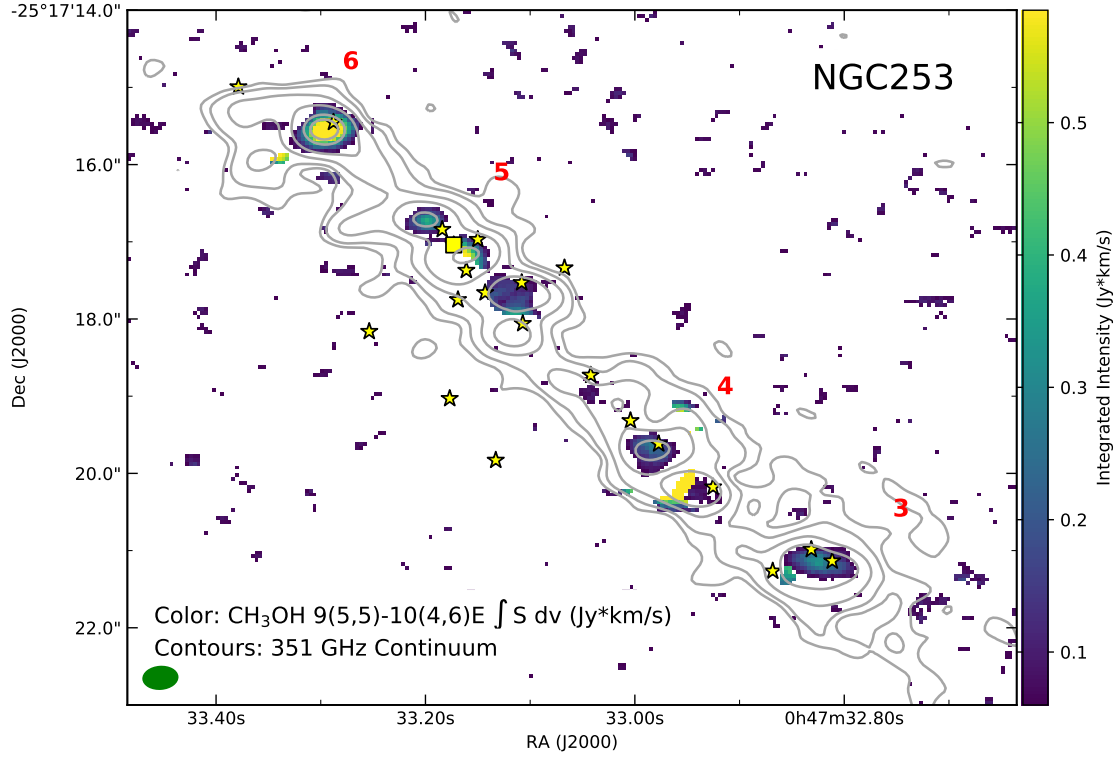**Figure 23.** CH_3CN $12-11$ integrated intensity.

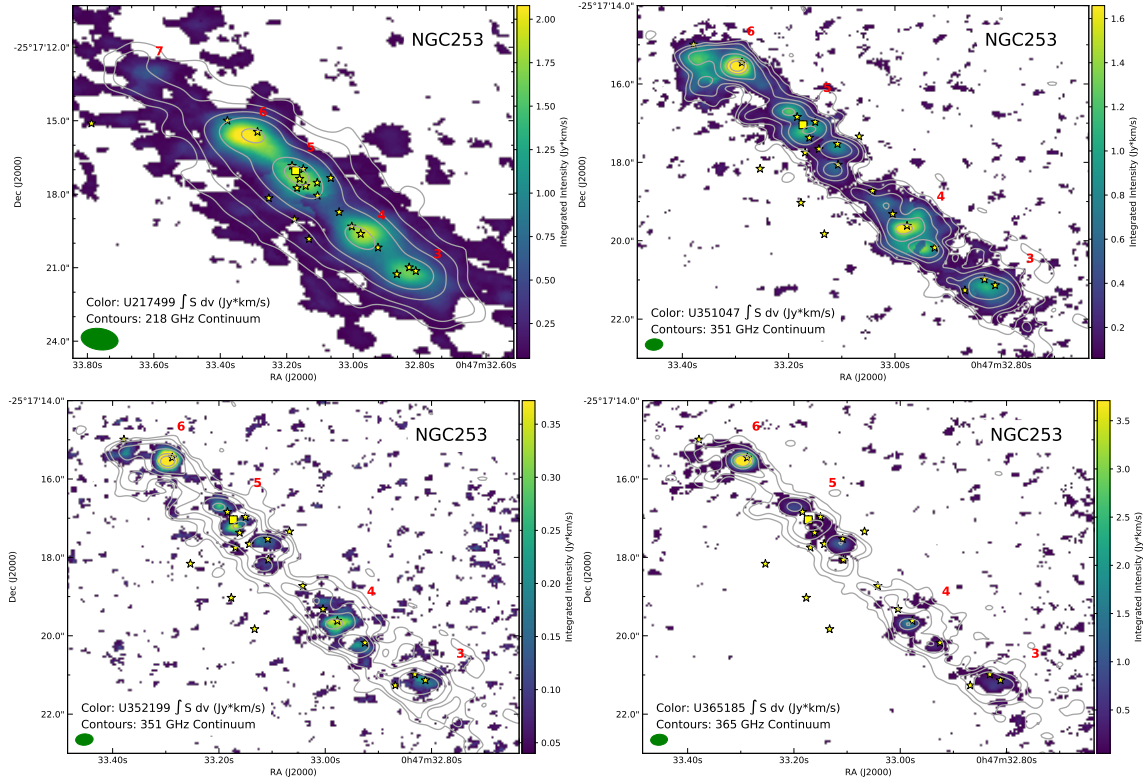**Figure 24.** CH$_3$OH $9_5 - 10_4E$ integrated intensity.

Figure 25. U217944 (top left), U351047 (top right), U352199 (bottom left), and U365185 (bottom right) integrated intensity.

Müller, T. G., Balog, Z., Nielbock, M., et al. 2016, A&A, 588, A109

Orton, G. S., Fletcher, L. N., Moses, J. I., et al. 2014, Icarus, 243, 494

Papadopoulos, P. P. 2010, ApJ, 720, 226

Pérez-Beaupuits, J. P., Güsten, R., Harris, A., et al. 2018, ApJ, 860, 23

Perley, R. A., & Butler, B. J. 2013, ApJS, 204, 19

Rekola, R., Richer, M. G., McCall, M. L., et al. 2005, MNRAS, 361, 330

Rieke, G. H., Lebofsky, M. J., Thompson, R. I., Low, F. J., & Tokunaga, A. T. 1980, ApJ, 238, 24

Rieke, G. H., Lebofsky, M. J., & Walker, C. E. 1988, ApJ, 325, 679

Robitaille, T., Ginsburg, A., Beaumont, C., Leroy, A., & Rosolowsky, E. 2016, spectral-cube: Read and analyze astrophysical spectral data cubes, Astrophysics Source Code Library, ascl:1609.017

Rosenberg, M. J. F., van der Werf, P. P., & Israel, F. P. 2013, A&A, 550, A12

Sakamoto, K., Mao, R.-Q., Matsushita, S., et al. 2011, ApJ, 735, 19

Shirley, Y. L. 2015, Publications of the Astronomical Society of the Pacific, 127, 299

Sobolev, V. V. 1960, Moving Envelopes of Stars (Cambridge: Harvard University Press, 1960)

Teuben, P., Pound, M., Mundy, L., et al. 2015, in Astronomical Society of the Pacific Conference Series, Vol. 495, Astronomical Data Analysis Software an Systems XXIV (ADASS XXIV), ed. A. R. Taylor & E. Rosolowsky, 305

The Astropy Collaboration, Price-Whelan, A. M., Sipőcz, B. M., et al. 2018, ArXiv e-prints, arXiv:1801.02634

Tiemann, E. 1974, Journal of Physical and Chemical Reference Data, 3, 259

Turner, J. L., & Ho, P. T. P. 1985, ApJL, 299, L77

Ulvestad, J. S., & Antonucci, R. R. J. 1997, ApJ, 488, 621

van der Tak, F. F. S., Black, J. H., Schöier, F. L., Jansen, D. J., & van Dishoeck, E. F. 2007, A&A, 468, 627

van der Tak, F. F. S., & van Dishoeck, E. F. 2000, A&A, 358, L79

Weaver, K. A., Heckman, T. M., Strickland, D. K., & Dahlem, M. 2002, ApJL, 576, L19

Weiland, J. L., Odegard, N., Hill, R. S., et al. 2011, ApJS, 192, 19

Weiß, A., Kovács, A., Güsten, R., et al. 2008, A&A, 490, 77

Wyrowski, F., Schilke, P., & Walmsley, C. M. 1999, A&A, 341, 882

Xu, L.-H., & Lovas, F. J. 1997, Journal of Physical and Chemical Reference Data, 26, 17